Computers and Geotechnics 152 (2022) 104992

Contents lists available at ScienceDirect

Computers and Geotechnics

journal homepage: www.elsevier.com/locate/compgeo

CDEM-based simulation of the 3D propagation of hydraulic fractures in heterogeneous Coalbed Methane reservoirs

Qingshan Ren [a], Yixin Zhao [a,*], Xinguang Zhu [c,d], Yu Zhou [c,d], Yaodong Jiang [b], Pengpeng Wang [a], Cun Zhang [a]

[a] School of Energy and Mining Engineering, China University of Mining and Technology(Beijing), Beijing, China
[b] School of Mechanics and Civil Engineering, China University of Mining and Technology(Beijing), Beijing, China
[c] Institute of Mechanics, Chinese Academy of Sciences, Beijing 100190, China
[d] University of Chinese Academy of Sciences, School of Engineering Science, Beijing 100049, China

ARTICLE INFO

Keywords:
Continuous discontinuous element method (CDEM)
Discrete fracture network (DFN)
Volume heterogeneity
Maximum fracture width
Multivariate regression analysis

ABSTRACT

To simulate the propagation law of hydraulic fractures in deep Coal Bed Methane (CBM) reservoirs in Qin-shui basin, a 3D numerical model is established using a continuous-discontinuous algorithm, and a discrete fracture network (DFN) is included in the model to increase its heterogeneity. The control variable method was employed to study the effects of in situ stress, random fracture number, fracturing fluid flow and viscosity on hydraulic fracture propagation. The results show that the fracture surface of hydraulic fracture can extended rapidly to the upper and lower boundaries of the model, and then extend to the two ends perpendicular to the minimum principal stress. Simultaneously, there was also a short-distance extension along the direction of the minimum principal stress. The fracture width in the horizontal section is oval, that is, the fracture width at the injection point is the largest, and the fracture width decreases gradually in the process of extending forward. The pressure data of the fracturing fluid also decrease gradually along the expansion process. With an increase in the buried depth of the coal seam, the fracture pressure of hydraulic fracture sharply increases, while the width of fracture sharply decreases. The random fracture in the model will be conducive to the expansion of hydraulic fracture only when the angle between its strike angle and the maximum horizontal principal stress is very small and will "hinder" the expansion of hydraulic fracture in most cases. The greater the density of random fractures in the reservoir is, the more obvious the "blocking" effect and the smaller the fracture width of hydraulic fractures. The increase in the fracturing fluid injection flow can significantly affect the propagation speed and width of hydraulic fractures. The increase in the fracturing fluid viscosity will change the shape of hydraulic fractures from "oval" to "round", which is not conducive to the expansion of hydraulic fractures. Volume heterogeneity is introduced to quantitatively determine the heterogeneity characteristics of the model, and multiple regression analysis is used to obtain the relationship among hydraulic fracture length, maximum fracture width and volume heterogeneity, buried depth, injection flow and injection time when low viscosity water is used as fracturing fluid. It is determined that the volume heterogeneity of coal reservoirs, burial depth (in situ stress), fracturing fluid flow rate and viscosity are the main controlling factors affecting the fracture length and maximum fracture width.

1. Introduction

The bottleneck problem of deep exploitation of coalbed methane is low gas production and rapid attenuation, while the permeability of deep coalbed methane reservoirs is low, which will substantially hinder the analysis and diffusion process of coalbed methane. The key measures for increasing the permeability of coalbed methane development are to use hydraulic fracturing technology to fracture the coal seam and create a resolution channel for the gas and to use drainage to reduce the reservoir pressure, to realize the "resolution-diffusion-percolation" process of coalbed methane and to transport it from the wellbore to the surface pipeline network (Ju et al. 2016; Kresse et al. 2013; Li et al. 2020) to increase the contact area of hydraulic fracture and the reservoir, it is necessary to increase the complexity of fracture as much as

* Corresponding author.
E-mail address: zhaoyx@cumtb.edu.cn (Y. Zhao).

https://doi.org/10.1016/j.compgeo.2022.104992
Received 12 May 2022; Received in revised form 18 August 2022; Accepted 20 August 2022
Available online 7 September 2022

possible and to form a fracture network. (Lyu et al. 2020; Palmer 2010; Peng et al. 2009).

The development of coalbed methane faces many difficulties, one of which is the propagation law of hydraulic fractures (HF) in deep coal reservoirs (Lyu et al. 2020; Palmer 2010; Peng et al. 2009). Compared with other rock masses, the strength of the coal rock mass is lower, and multilevel structures such as fractures, bedding and cleats are internally developed. The heterogeneity of the coal rock mass is obvious, accompanied by mechanical characteristics such as a low elastic modulus and high Poisson's ratio (Ai et al. 2018; Cheng et al. 2018; Jiang et al. 2019; Jiang et al., 2016). The unique structural and mechanical properties of the coal rock mass cause the hydraulic fracture extension in the coal rock mass to substantially differing from the hydraulic fracture characteristics in other hard rocks (Ai et al. 2018; Cheng et al. 2018; Jiang et al. 2019; Jiang et al., 2016). The extension mechanism of coal seam hydraulic fracturing and the fine description of fracture morphology have always been difficult to research. Presently, there is still a lack of accurate and appropriate methods for describing the expansion law of deep coal seam hydraulic fractures (Huang et al., 2017a; Huang et al., 2017b; Wu et al. 2020).

Many scholars worldwide have investigated the hydraulic fracture extension of coalbed methane reservoirs, and the research methods include theoretical analysis, geophysical probing, laboratory experiments and numerical analysis (Carrier and Granet 2012; Dahi-taleghani and Olson 2011). The results of theoretical analysis are based on the elastic homogeneous model, which has limited guiding significance for the fracture propagation of heterogeneous rock masses in complex stratigraphic environments. Field physical exploration can only roughly judge the extension direction and length of the main hydraulic fracture. The test blocks of indoor experiments are often concentrated in the range of small side lengths. Numerical simulation has many advantages over the above methods, such as visualization and repeatability, so the numerical simulation technology of hydraulic fracturing has been rapidly developed.

The numerical analysis of hydraulic fracturing has experienced a development process from two-dimensional to three-dimensional. Scholars worldwide have proposed a variety of numerical simulation methods, such as the finite element method (FEM), discrete element method (DEM), boundary element method (BEM), displacement discontinuity method (DDM), and extended finite element method (EXFM)(Carrier and Granet 2012; Chen et al. 2017; Dou et al. 2019; Ju et al., 2018b; Li et al. 2020; Wang 2019). Among them, the plastic criterion of finite element method mostly adopts Mohr Coulomb equal strength criterion; the crack extension mostly assumes the extension path; the fracture extension is mostly a simple crack; and the complex crack mesh is rarely considered (Chen 2012; Dahi-taleghani and Olson 2011). The discrete cell method can achieve arbitrary path expansion of hydraulic fractures through random grids to a certain extent, and the computational accuracy is not as high as the finite element accuracy (Chen 2012; Dahi-taleghani and Olson 2011). The extended finite element method can consider the crack propagation of any path, but it needs implicit iteration, which renders the calculation of large-scale problems difficult, and the number of conditions of the algorithm is high, which easily leads to divergence (Chen 2012; Dahi-taleghani and Olson 2011). The DDM is used to simulate hydraulic fracturing, in which fluid can flow through closed natural fractures but the permeability of the rock itself is still not considered (Lecampion and Detournay 2007). The boundary element method transforms the volume operation into a boundary operation. The fracture propagation path is limited, so the simulation of hydraulic fracturing under any path is difficult. At the same time, this method cannot calculate a complex medium model, which seriously limits the scale of the research model (Ju et al., 2018b; Zhang et al. 2015).

A natural rock mass is composed of multiple groups of joint weak planes and blocks, that is, the material contains continuous and discontinuous units. In the numerical calculation, the finite element method is employed to calculate the continuous medium of the element block; the mechanical state inside the element block is obtained; and the discrete element method is utilized to calculate the mechanical state of the block boundary. The motion characteristics between two blocks are calculated according to the spring theory. This solution method realizes the combination of continuous deformation of continuous materials and progressive change failure of discontinuous materials, which is referred to as the continuous discontinuous element method and can be reasonably applied to numerical simulation in many fields (Chuang et al., 2017; Li et al. 2015; Ma et al. 2016; Wang et al. 2019). Discrete fracture network (DFN) modeling technology constructs a model of rock masses with complex fractures through the complex interaction of various fracture networks distributed in three-dimensional space, which can realize the detailed description of fracture systems from geometric form to seepage behavior (Jung, Fenwick, and Caers 2013; Marongiu-Porcu et al. 2016; Ren et al. 2017). The establishment of a discrete fracture network model and the numerical calculation of hydraulic fracturing by the continuous discontinuous element method can describe the propagation law of hydraulic fractures in fractured rock masses in detail. In this paper, the method of adding random weak surface structure to the model to increase the heterogeneity of the model to a certain extent increases the heterogeneity of the model, but limited by the lack of computing power, the heterogeneity of the model in this paper is still very small compared with the heterogeneity of coal reservoir in nature. By gradually increasing the model heterogeneity value to fit the relationship between key hydraulic fracture parameters and heterogeneity degree, the problem of small heterogeneity of the model is remedied to some extent.

The structure of this paper is organized as follows: First, the fluid–solid coupling algorithm in the continuous discontinuous numerical simulation method is introduced. Second, a coal reservoir model with DFN random fractures is established by using the above algorithm software, and hydraulic fracturing numerical analysis is carried out by using the control variable method. Third, the relationship between multiple parameters and the hydraulic fracture length and maximum fracture width is fitted, and the influence of each variable on hydraulic fracture propagation in coal reservoirs is discussed. Last, the full text is summarized.

2. CDEM introduction

CDEM software is a numerical calculation software with independent intellectual property rights developed by Beijing Ji-Dao Cheng-ran Technology Co., ltd. and the Institute of Mechanics, Chinese Academy of Sciences. The software adopts a continuous discontinuous algorithm as the core algorithm. The algorithm combines the advantages of discrete elements and finite elements, analyzes the progressive failure of materials through the fracture of block boundaries and block interiors, and simulates the whole process from continuous deformation to crack generation and propagation (Lin et al., 2021). The algorithm software applies GPU technology to the calculation, which greatly improves the calculation ability (Ju et al. 2016; Ma et al. 2011).

2.1. Solid deformation-fracture solution

There are two important basic models in the CDEM computational model: the block model and interface model. The block can be composed of one or more finite element elements used to characterize the continuous characteristics of a material. The contact surface between two blocks and between two finite element elements in the blocks is defined as the interface, which is applied to characterize the discontinuous characteristics of the material. The interface consists of a real interface and virtual interface. The real interface refers to the interface between two blocks, representing the weak surface or potential fracture position between two blocks, and the virtual interface refers to the interface between two units in blocks. The connection between the

blocks is made by a contact spring connection, and the continuous fracture of the contact spring represents the fracture extension process of the simulated material. The CDEM calculation model is shown in Fig. 1. The schematic includes five blocks, in which the boundary of the block (red interface) represents the real interface and the interior of the block (black interface) represents the virtual interface.

In a rock body that contains fractures, the fluid can deeply penetrate the rock body along the joints, so in the CDEM fluid–solid coupling calculation, we assume that the fluid exists in the rock joints and adopt the solid unit method to calculate the continuous medium field by calculating the fracture seepage field through the fracture units that exist on the adjacent surfaces between two solid units, which can realize the numerical calculation of the fluid–solid coupling in the fractured rock body.

2.1.1. Solution of the block model

The material in the CDEM block element is considered a continuous homogeneous material, which is a finite element. The governing equation of the finite element can be expressed as.

$$M\ddot{u}^e + C\dot{u} + Ku^e = F^e \tag{1}$$

where M represents the total mass matrix, C represents the damping matrix, K represents the element stiffness matrix, u^e represents the element displacement vector, and F^e represents the external force on the element, including the solid force and fluid pressure.

In the time domain, Euler's forward difference method is employed to obtain an explicit iterative solution. The form is expressed as follows:

$$\begin{cases} \dot{u}^{n+1} = \dot{u}^{n+1} + \ddot{u}\Delta t, \\ u^{n+1} = u^{n+1} + \dot{u}\Delta t. \end{cases} \tag{2}$$

2.1.2. Solution of the interface model

The interface between the finite elements in the blocks is used to characterize the discontinuity of the materials. The relationship between the relative displacement of the contact points of adjacent elements and the spring force satisfies Hooke's Law:

$$\begin{cases} \Delta u_n = \dfrac{F_n}{K_n} = \dfrac{(\sigma_{n1} + \sigma_{n2})A}{2K_n} \\ \Delta u_\tau = \dfrac{F_\tau}{K_\tau} = \dfrac{(\sigma_{\tau 1} + \sigma_{\tau 2})A}{2K_\tau} \end{cases} \tag{3}$$

where $\triangle u_n$ and $\triangle u_\tau$ are the normal relative displacement and tangential relative displacement, respectively; F_n and F_τ are the normal force and tangential force, respectively; σ_{n1} and σ_{n2} are the normal stresses of the contact point; $\sigma_{\tau 1}$ and $\sigma_{\tau 2}$ are the tangential stresses at the contact point; K_n and K_τ are the normal stiffness and tangential stiffness, respectively, of the spring; and A is the area of the contact point.

The maximum tensile stress criterion and Mohr-Coulomb criterion serve as the failure criteria of the materials. When the normal stress of the contact point pair satisfies the following formula:

$$\sigma_n \geqslant \sigma_t \tag{4}$$

tensile failure occurs to the material, and the normal force of the contact point pair is corrected to $F_n = 0$. In the above formula, σ_τ is the tensile strength of the contact surface. When the tangential stress of the contact point pair is satisfied.

$$\sigma_\tau \geqslant c + \sigma_n \tan\phi \tag{5}$$

The material will suffer shear failure, and the tangential force of the contact point pair will be modified to $F_\tau = F_n \tan\phi$.

2.2. Coupled solution of the 3D rock flow field and fracture

The solution process follows the following assumptions: the permeability of fractures or joints is characterized by fracture seepage and follows the cubic law. The idea of fluid structure coupling in the CDEM is shown in Fig. 2.

The fluid flow in the fracture will exert fluid pressure on the solid units on either side of it. The adjacent solid units will be opened and closed under the action of fluid pressure and external load. The change in the relative displacement between two solid elements will affect the opening of the crack. According to the cubic law, a change in the fracture opening will result in a change in fluid pressure.

When the saturation accumulation of the node is 1, the fluid pressure P_p can be calculated according to Eq. (6).

$$p_p = -\sum_{t=0}^{t}\left(k^F \frac{(Q^F + Q_{app})}{nV}\Delta t\right) \tag{6}$$

where k^F Permeability coefficient of fracture (m^2/Pa.s); Q^F Flow rate of node of fracture ($m^3.s^{-1}$); $Qapp$ is the external flow boundary condition; Δt is the calculation step, n is the porosity; V is the volume of fracture element node; n is the porosity; V is the volume of fracture element node.

Next, the total node pressure can be expressed as.

$$P^F = p_p - \overline{s^F}\rho_e(xg_x + yg_y + zg_z) \tag{7}$$

where ρ_e is the fluid density; g_x, g_y and g_z are the overall components of gravity acceleration; x, y and z are the three components of the overall coordinates of the node, and $\overline{s^F}$ is the saturation of the fracture element.

By introducing the fluid pressure PF into Equation (8), the updated node displacement of the solid element (U_{Ai} , U_{Bi} , and $i = 1, 2,$ and 3, as shown in Fig. 3) can be obtained to calculate the solid stress field and seepage field. The fracture opening w_i can be calculated by the following formula:

$$w_i = |U_{Ai} - U_{Bi}|, i = 1, 2, 3, \tag{8}$$

where U_{Ai} is the coordinate vector of the three nodes on the upper surface of entity unit a and U_{Bi} is the coordinate vector of the three nodes on the bottom surface of entity unit b. The fluid pressure can be updated by Equations (6) and (7).

The calculation of fracture seepage meets the cubic law:

$$Q^T = -\frac{w^3}{12\mu}\frac{\Delta p}{l} \tag{9}$$

where Q^T represents the flow through the fracture, μ represents the

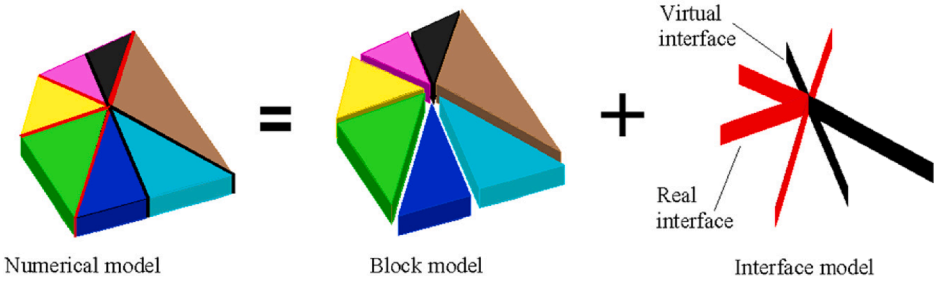

Fig. 1. Schematic of CDEM.

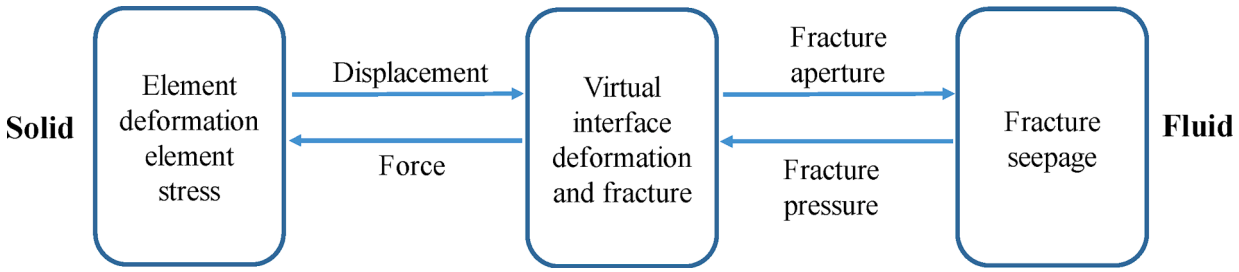

Fig. 2. Coupling idea of the CDEM.

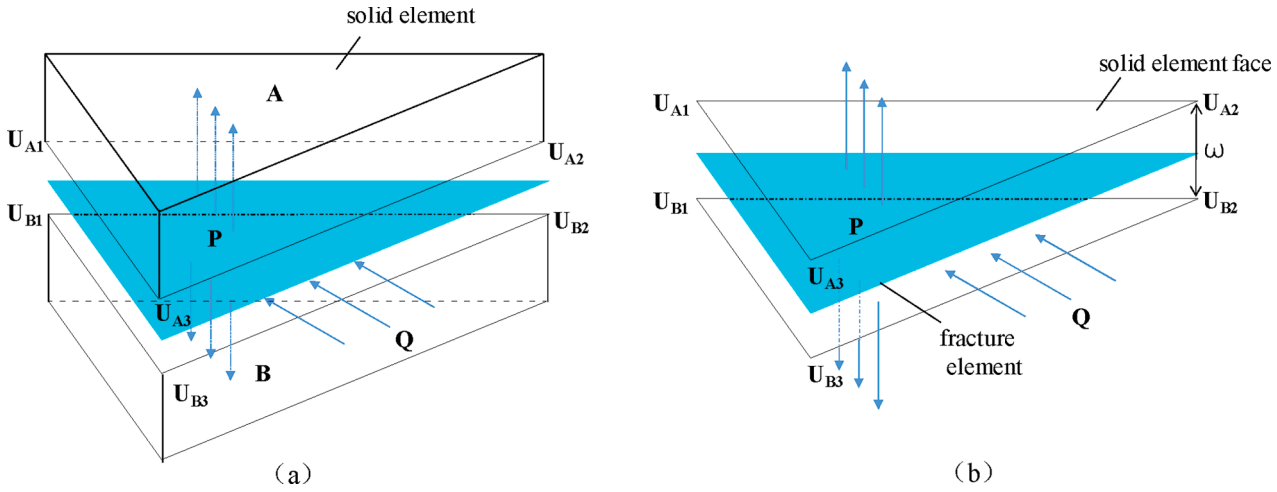

Fig. 3. Diagram of the solid-fracture seepage coupling algorithm.

hydrodynamic viscosity, $\triangle P$ represents the pressure difference, w represents the crack opening, l represents the fracture length.(Zhu et al. 2021).

2.3. Principle of hydraulic fracture propagation in CDEM

As shown in Fig. 4, Fig. 4 (a) is the schematic diagram of fracture propagation (De Pater 2015). During fracture propagation, the tip of hydraulic fracture forms a cohesive zone, and both sides of the crack tip are high shear stress zones. Due to the opposite direction of shear stress on both sides of the fracture, the fracture of the material in this area occurs. Fig. 4 (b) is the hydraulic fracture simulated by CDEM, which corresponds to Fig. 4 (c) is the shear stress cloud diagram of solid units at both ends of the fracture in the matrix on both sides of the fracture. It can be seen from the Figure that high shear stress zones appear at both ends of the fracture. The direction of shear stress on both sides of the high shear stress zone is also opposite. The stress in the opposite direction causes the crack enlargement at the grid interface of the fracture tip and the fracture of the joint connection spring, and the fracture expands forward with the continuous injection of fracturing fluid.

3. Numerical model

3.1. Selected models

This model adopts CDEM fluid–structure coupling algorithm, and refers to the stress distribution and occurrence of #15 coal seam in the Qin-shui basin. The size of the model is set to 30 m × 30 m × 6 m. The

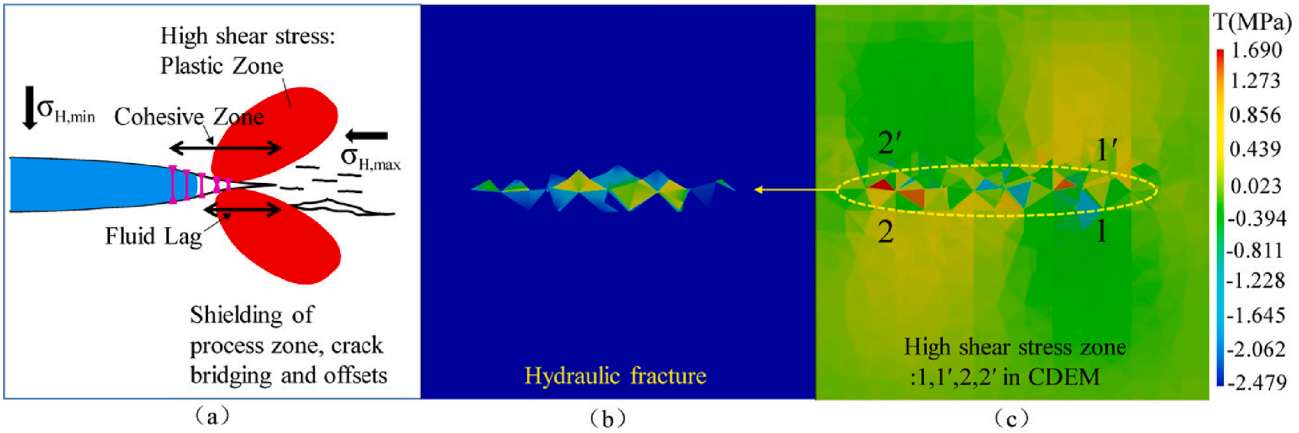

Fig. 4. Cloud image of high shear stress area at hydraulic fracture tip in CDEM.

design of different numbers of fracture surfaces in the model is realized through code setting (refer to Section 3.2 for details). As shown in Fig. 5 (d), the model is divided into fracture seepage units composed of contact surfaces of about 20,080 tetrahedral elements and 39,080 tetrahedral elements through mesh division. The constitutive model of tetrahedral elements are set as linear elastic constitutive model, and the constitutive model of fracture seepage element is set as Mohr-Coulomb constitutive model of brittle fracture. The injection point of the model is located in the volume center of the model, as shown in Fig. 5 (c), the endpoint at the lower left corner of the model is set as the origin of coordinates, and the position of the injection point is the grid node closest to the coordinate point (15,15,3), The fracturing fluid injection mode is selected as the constant flow mode.

3.2. Generation of a discrete fracture network (DFN)

The DFN random fracture model adopts an object-oriented, geostatistical modeling method, and the model object parameters are random and discrete. As shown in Fig. 5(a), in this model, random circular surfaces are generated by compiling codes to represent the weak surface structure in a natural rock mass (NF). Each geometric surface has position, direction, shape, thickness, etc. In the spatial distribution of geometric surfaces, each geometric surface is usually randomly located, and the generation of random parameters conforms to the law of a Weibull probability distribution. As shown in Fig. 5(b), after the number of discs is set in this model, the center coordinates are randomly generated, and the upper and lower limits of the radius are set to [0.3 m, 1 m]. For the trend of the fracture surface, the angle between the diameter AB parallel to the XY plane and the X axis β is set to β. The value range is [0°, 180°]. The inclination angle α is the angle between the fissure surface and the XY plane, and the value range of α is set to [0°, 90°].

3.3. Parametric selection

Referring to the previous research results on the mechanical properties of the No. 15 coal in the Qin-shui basin, the model numerical parameters shown in Table 1, including the mechanical parameters and pore properties of #15 coal, are obtained through screening. In the model, the fracturing fluid uses clean water (Lyu et al. 2020; Wang et al. 2020).

The analysis of the characteristics of deep geostress in the Qin-shui basin shows that the overall geostress in the Qin-shui basin is characterized by "shallow dispersion and deep convergence" (Zhang et al. 2020b; Zhang et al. 2019; Zhaoxia et al., 2020). There is a critical depth between 640 m and 825 m in the shallow and deep parts. The critical depth is generally characterized by the distribution of a deep in situ stress $\sigma_H > \sigma_v > \sigma_h$ state, as shown in Fig. 6. Through numerical fitting analysis, it can be concluded that the relationship between the maximum horizontal principal stress and the burial depth meets the

Table 1
Input parameters for simulating hydraulic fracture propagation.

Parameters	Value
Density of intact coal	1400 kg/m^3
Young's modulus	3.5 GPa
Poisson's ratio	0.30
Permeability coefficient of intact coal	1E-15
Porosity of intact coal	5 %
Specific weight of injection fluid	9800
Fluid viscosity	1E-3 Pa·s
Tensile strength of intact coal	3 MPa
Cohesive force of intact coal	3 MPa
Interior friction angle of intact coal	35°
Dilatancy angle of intact coal	15°
Injection rate	50 ml/s

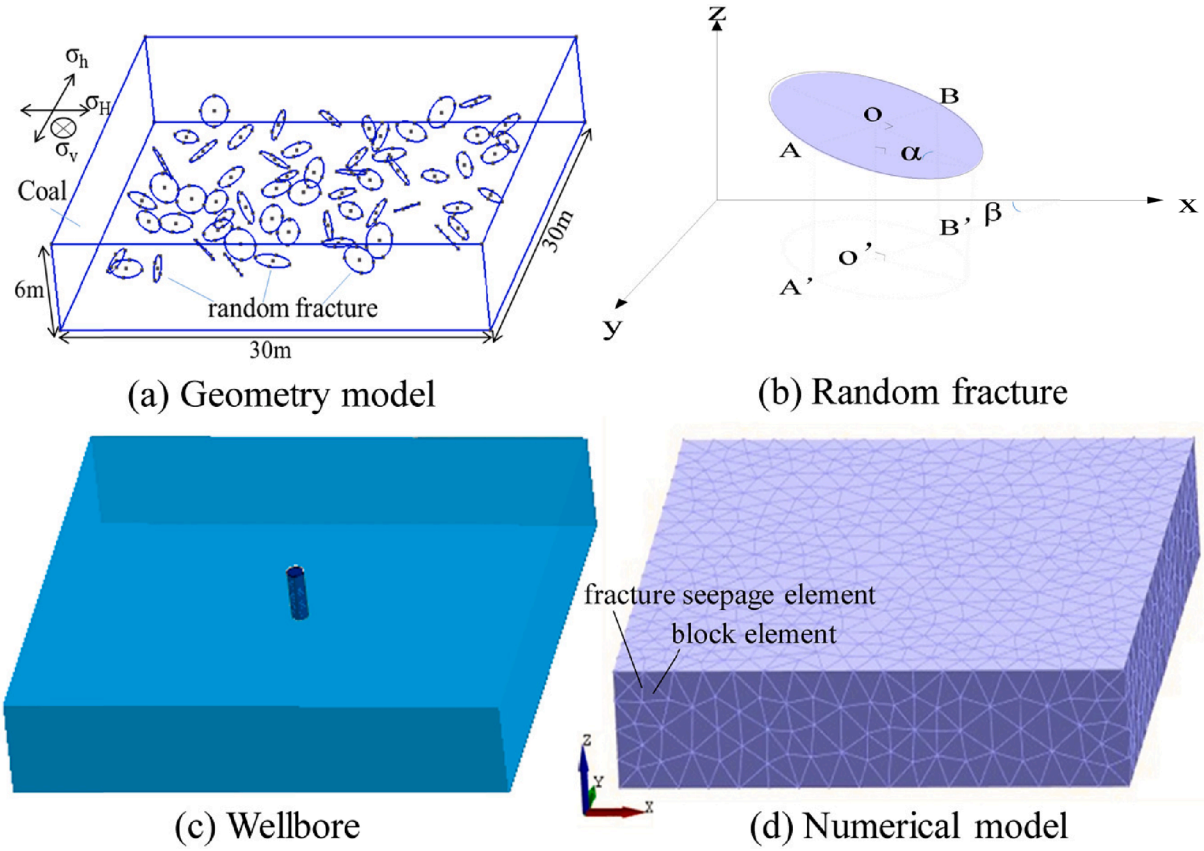

Fig. 5. Numerical model with random fractures.

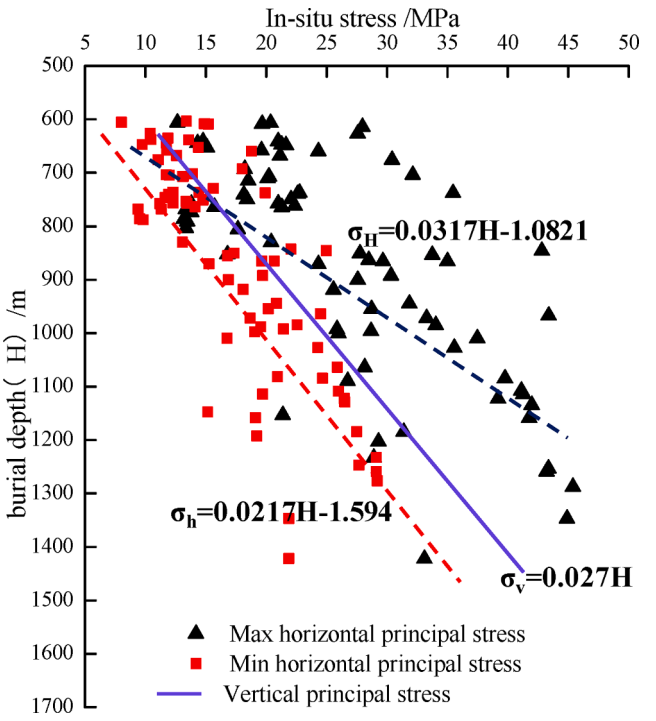

Fig. 6. In situ stress of the deep coalbed methane reservoir in the Qin-shui Basin (Zhang et al. 2020b; Zhang et al. 2019; Zhaoxia et al. 2020).

requirements σ_H = 0.0317H-1.0821. The relationship between the minimum horizontal principal stress and burial depth satisfies σ_h = 0.0217H-1.594. The intermediate principal stress is derived from the gravity of the overlying strata σ_v = 0.027H. Five groups of stress values with burial depths of 600 m, 800 m, 1000 m, 1200 m and 1400 m are used. The maximum horizontal principal stress is loaded in the X direction; the minimum horizontal principal stress is loaded in the Y direction; and the vertical stress is loaded in the Z direction.

3.4. Numerical calibrations

(Zhu et al. 2021) for the first time conducted parameter calibration for three-dimensional hydraulic fracturing numerical model using CDEM. Based on the case of radial hydraulic fracturing, the validation model verifies the accuracy of fracture opening, length and fracture morphology under fluid drive. The numerical model as shown in Fig. 7 (a) was established with a size of 200 m × 200 m × 240 m, which was divided into 79,657 tetrahedral elements. The average element size at the fracture plane as shown in Fig. 7(b) was 3 m. Material parameters are as follows: dynamic viscosity $\mu = 1.67 \times 10^{-2}$ Pa.s, E = 20 GPa, σ_t = 0.54 MPa. The initial compressive stress of the model was set as 10 MPa, the transverse flow of fixed point source was loaded for 1000 s, and the flow value was 0.01 m^3/s. The numerical simulation results of crack opening cloud map were shown in Fig. 7(c), and the final crack propagation radius was 52.87 m. Compared with 3DEC simulation results (Fig. 7(d)), the error is 0.4 %(Dontsov and Zhang. 2018). A horizontal line was set at the center of the fracturing surface in the horizontal direction. After calculation, the fracture opening at the final moment of the horizontal line was monitored and the curve was drawn as shown in Fig. 7(e). According to the Figure, the maximum fracture opening was 2.02 mm, and the maximum error was 1.0 % compared with the approximate solution in the literature. The results show that this method can accurately describe the fracture morphology under hydraulic fracturing. At the same time, the hydraulic fracturing simulation of layered shale was also carried out in the literature (Zhu et al. 2021). The same parameters and stress paths were assigned to the literature (Tan et al., 2017) and compared with the experimental results in the literature. The same fracture morphology was found in the two studies. The pore pressure curve at injection point of the model is in good agreement with the theoretical solution. These two models verify the validity of the numerical method being used in this study.

4. Numerical simulation results

The fracturing injection rate and viscosity, burial depth and number of random fractures in the model are selected as the main control variables to investigate the three-dimensional, extensional morphological characteristics of hydraulic fractures, pressure characteristics of hydraulic fractures, fracture length, maximum fracture width and other variation patterns with the control variables.

4.1. Fracture morphology and fluid pressure characteristics

The simulation parameters are set as shown in Table 1. The fracturing fluid flow is 7000 ml/min, and the viscosity is 0.001 Pa·s. The three-dimensional stress at a burial depth of 1000 m is selected as the formation stress. The three-dimensional, hydraulic fracture shape for 40 random fractures is shown in Fig. 8, which also shows the three-dimensional, expansion morphology of the hydraulic fracture obtained from the simulation at three different time points and the projection morphology of the hydraulic fracture in the XY, XZ and YZ planes at the same moment. The hydraulic fracture extends along the plane where XZ is located, that is, it extends along the direction of the maximum principal stress and passes through multiple fracture surfaces. The hydraulic fracture also extends a certain distance in the direction perpendicular to the maximum principal stress.

As shown in Fig. 9, a total of 5 fluid pressure monitoring points M_1-M_5 are set in the model; their coordinates are (15,15,3), (12,15,3), (9,15,3), (6,15,3), and (3,15,3). The fracturing fluid flow is 3000 ml/min, and the viscosity is 0.001 Pa·s. The formation stress selects the stress parameter at a burial depth of 1000 m. When the number of random fractures is 0, the flow pressure fluctuation curve of the monitoring points is shown in Fig. 9. Point M1 is the pressure curve of the fracturing fluid injection point, and there is an obvious breakdown pressure point on the pressure curve of point M_1. With the expansion of hydraulic fractures, the curve from M_1 to M_5 monitors the stable water pressure, and the water pressure from M_1 to M_5 gradually decreases. This finding is consistent with the variation characteristics of water pressure in the process of hydraulic fracturing described by other scholars in the paper. (Yan and Zheng 2017; Zhu et al. 2021).

4.2. Impact of buried depth

The simulation parameters shown in Fig. 10(a) are shown in Table 1, and the number of random fractures is 0. Fig. 10(a) shows the trend line of the breakdown pressure of the hydraulic fracture obtained from the simulation with burial depth. The breakdown pressure increases with an increase in the burial depth, and the breakdown pressure grows with burial depth in a natural exponential relationship. (Wanniarachchi et al. 2017) verified that in the hydraulic pressure experiment of shale, the fracture pressure increases linearly with an increase in burial depth, which is similar to the experimental conclusion of this paper. Fig. 10(b) shows the variation trend line of the model fracture degree with burial depth. The fracture degree is the ratio of the fractured unit surface to the total fracture unit surface. Fig. 10(b) shows that the fracture degree of the model gradually decreases with an increase in burial depth.

Fig. 11(a) shows the width change curve of hydraulic fractures in the expansion direction of hydraulic fractures. The injection point is at the maximum fracture width. The farther from the injection point, the smaller the width of the hydraulic fracture. With an increase in the injection time, the value of the maximum hydraulic fracture gradually increases, but the increase range increasingly narrows. As shown in

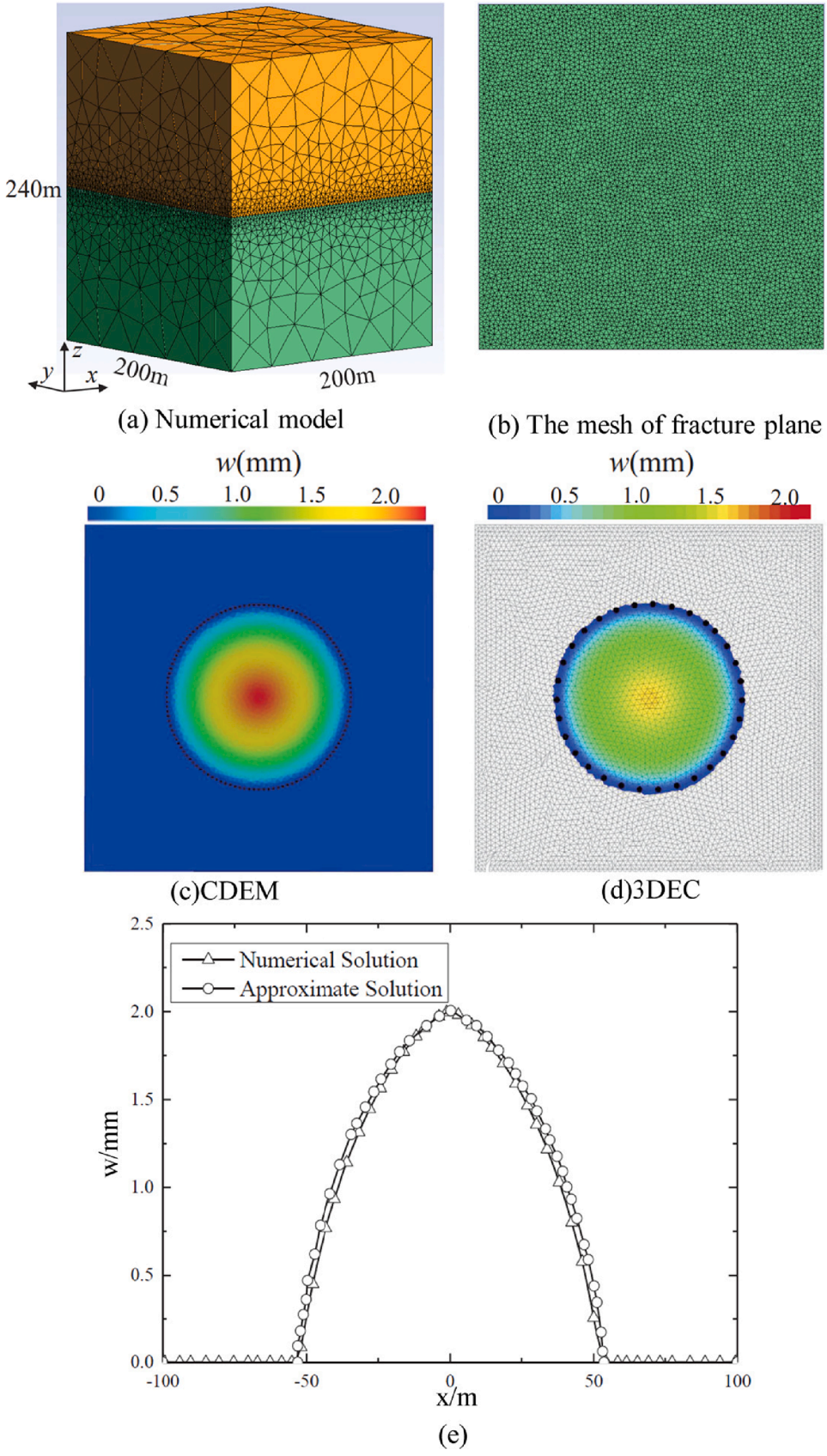

Fig. 7. Verification of CDEM 3d hydraulic fracturing numerical algorithm.

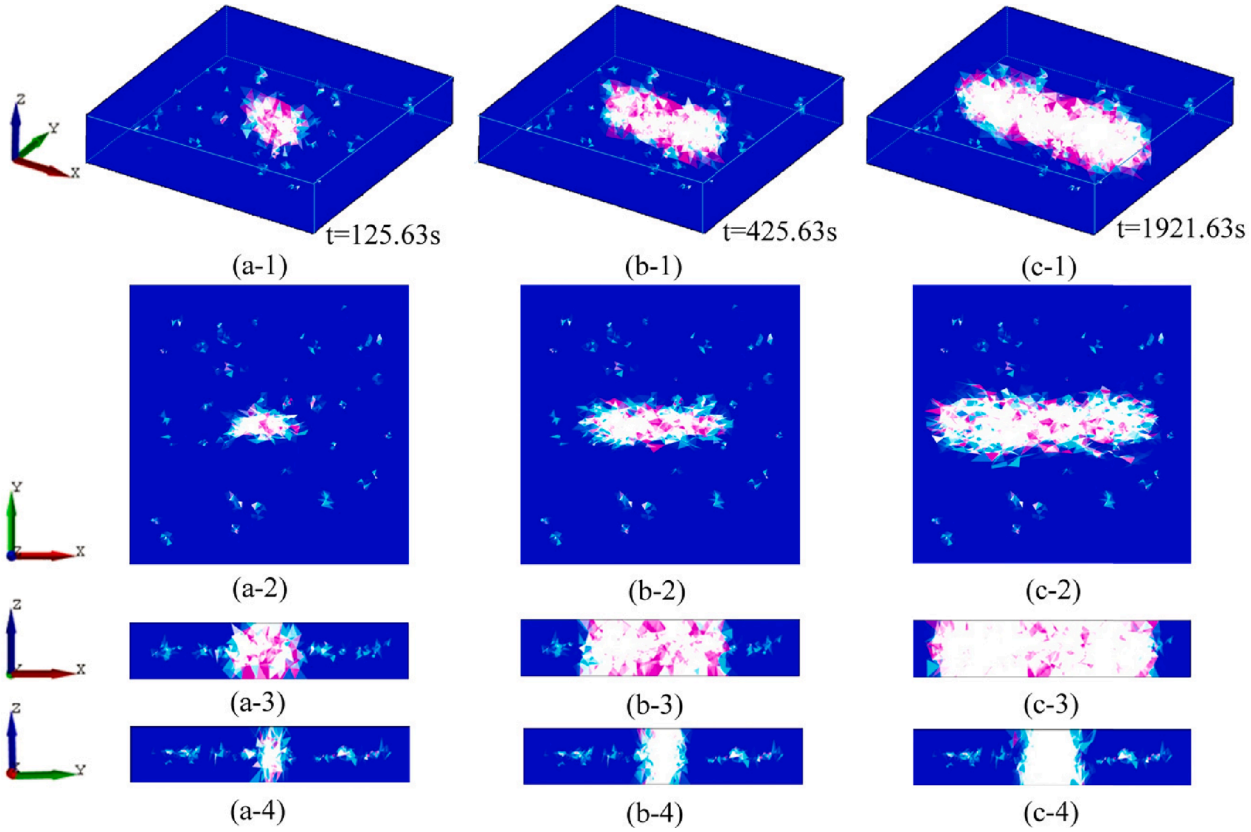

Fig. 8. Evolution of 3D hydraulic fracture morphology.

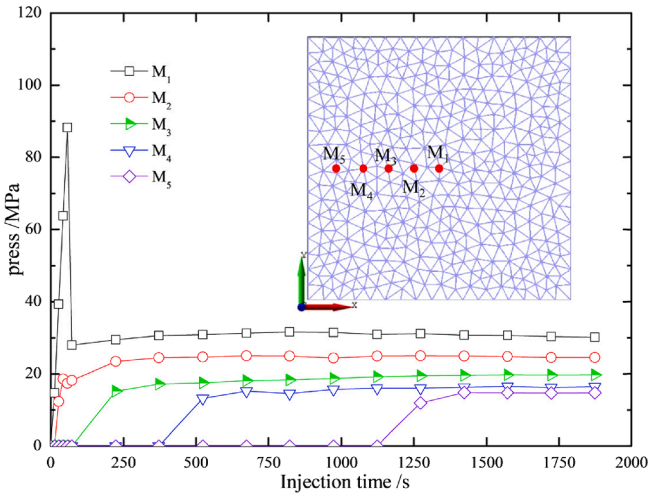

Fig. 9. Time history curve of injection pressure.

Fig. 11(b), when the injection time t = 2046.5 s, the maximum fracture width value of the model with different burial depths shows that the maximum fracture width of hydraulic fractures decreases with an increase in burial depth. When the burial depth increases from 600 m to 1400 m, the corresponding maximum hydraulic fracture width significantly decreases, from 62.05 mm to 21.24 mm, which is a decrease of approximately 61.71 %.Through indoor experiments, (Wanniarachchi et al. 2017) pointed out that a high ground stress difference hinders the expansion of hydraulic fractures, which is consistent with the research conclusion of this paper.

4.3. Impact of fracture

Natural fractures generally exist in the strata. The greater the complexity of the geological structure is, the stronger the heterogeneity of the reservoir, which will have a certain impact on hydraulic fracture propagation. Previous research results show that the effect of fracture structure on hydraulic fracturing can make hydraulic fractures stagnate, turn, or turn first and then pass through. As shown in Fig. 12, the XY plane is the hydraulic fracture propagation form of a single fracture surface, and the dotted line represents the weak surface position, which is on the path of hydraulic fracture propagation, with an approach angle of 90°. The rupture of the grid due to stress concentration will exist near the location of the fracture surface shown in the above Figure, and the hydraulic fracture will accelerate toward the location of the fracture surface when it encounters the fracture surface, as shown in Fig. 12(c). The fracture surface exhibits the characteristic of attracting the expansion of the hydraulic fracture. After encountering the fracture surface, the hydraulic fracture shows repulsive characteristics, which hinders the expansion of the hydraulic fracture in this direction. As shown in Fig. 12 (g), Fig. 12(H) and Fig. 12(I), the hydraulic fracture expands to the boundary where there is no fracture surface.

Fig. 13(a) shows that a single crack with approach angles of 0°, 15°, 30°, 45°, 60°, 75° and 90° is set for simulation separately. Only when the approach angle is 0° can the crack accelerate the propagation of hydraulic fractures. In the range of approach angles in the range of 30° ~ 90°, natural fractures have an obvious “blocking” role in the expansion of hydraulic fractures. This role means that in most cases, natural fractures will probably hinder the expansion of hydraulic fractures, and the obstruction effect is most obvious in the range of 45° ~ 75°.

In the stress environment of a 1000 m buried depth, 0, 20, 40, 60, 80 and 100 random fractures are set in the model to explore the influence of the number of random weak planes on hydraulic fracture expansion. The simulation results show that the number of primary fractures in the

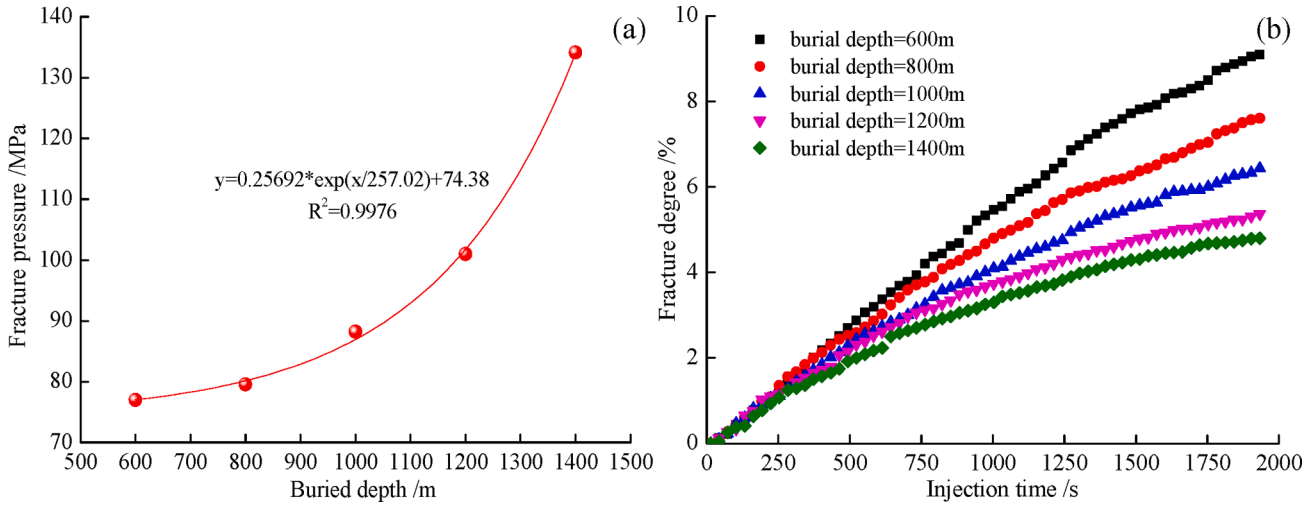

Fig. 10. Relation curve between breakdown pressure and fracture degree with burial depth.

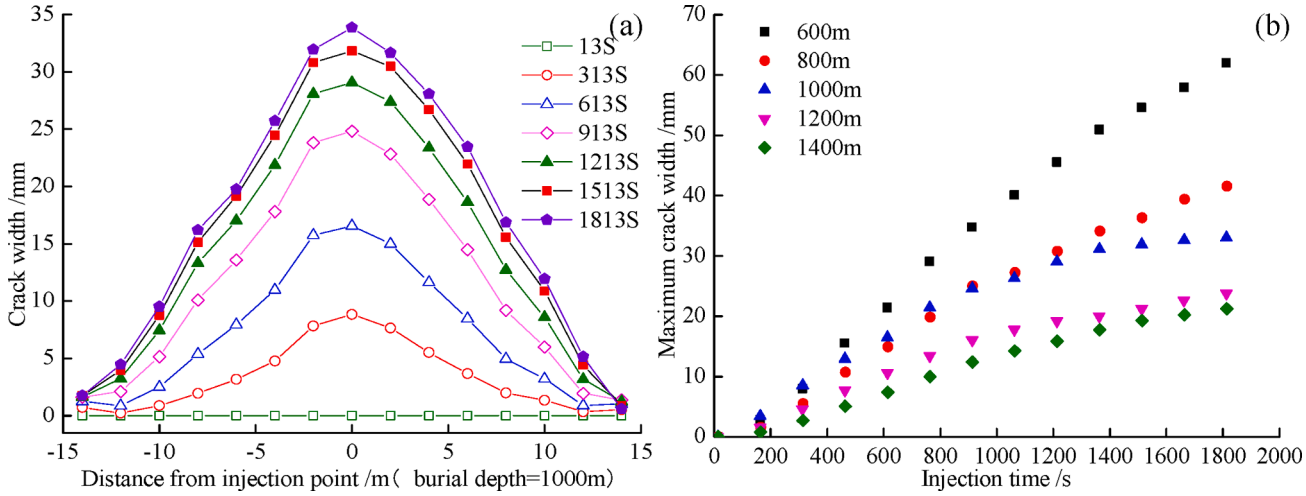

Fig. 11. Feature of hydraulic fracture width and relation curve with burial depth.

model has no obvious effect on the hydraulic fracture breakdown pressure, that is, the breakdown pressure is basically constant.

Fig. 13(b) shows that the density of the fracture surface can obviously hinder the forward expansion of hydraulic fractures. Therefore, it can be inferred that the more fractures there are in the reservoir and the greater the homogeneity is, the more difficult the expansion of hydraulic fractures will be. The research of paper (Wanniarachchi et al. 2017) shows that there is no obvious effect between the short fractures in the reservoir and the main fractures in the reservoir. Fracturing in this kind of CBM reservoir is not conducive to the extension of fractures and the exploitation of CBM. (Wanniarachchi et al. 2017) also shows that the original cracks in the rock mass will have a great impact on the new cracks.

As shown in Fig. 14(a), the increase in the number of fracture surfaces causes an increase in the material heterogeneity of the model, and the maximum fracture width will be significantly reduced. After the hydraulic fracture meets the fracture surface, part of the fracturing fluid will be filtered into the fracture surface, causing a sudden drop in water pressure. As shown in Fig. 14(b), with an increase in the number of fracture surfaces in the model, the hindering effect on the forward propagation of the fracture increases, which reduces the fracture degree of the model to a certain extent. (Chong et al. 2017; S. Wang, Li, and Li 2018).

4.4. Impact of the injection rate

The three stresses of the model are set as the stress at a depth of 1000 m; the number of random fracture surfaces is set to 40; and the other parameters of the model are listed in Table 1. The flow was set to 1000 ml/min, 3000 ml/min, 5000 ml/min, 7000 ml/min and 9000 ml/min. The numerical analysis results show that the increase in flow will cause an increase in the breakdown pressure. The data fitting results show that there is a natural exponential relationship between breakdown pressure and fracturing fluid flow Fig. 15(a).

There is a significant positive correlation between fracture propagation and fracturing fluid injection flow. The larger the injection flow is, the faster the fracture propagation speed is. As shown in Fig. 15(b), the fracture length propagation distance with an injection flow of 9000 ml/min is approximately 3 times that with an injection flow of 1000 ml/min

With the continuous injection of fracturing fluid, the simulation results show that the maximum fracture width of the numerical fracture increases with an increase in injection time and injection flow. In terms of increase amplitude, the increment of the maximum fracture width of the crack becomes increasingly slower (Fig. 16(a)). Fig. 16(b) shows that with an increase in fracturing fluid flow, the propagation speed and maximum fracture width of the hydraulic fracture increase, and the fracture degree of the model significantly increases. Through laboratory

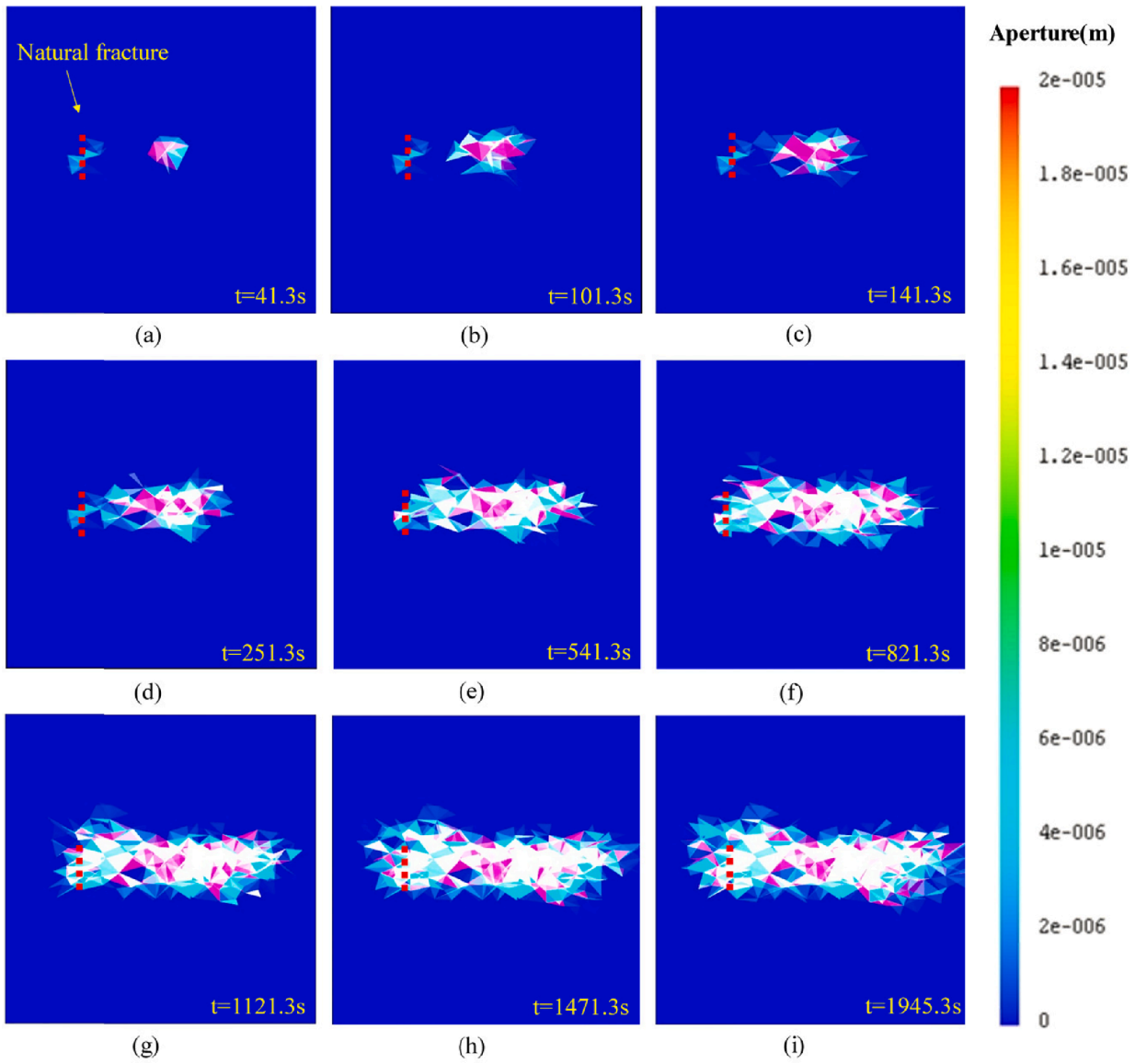

Fig. 12. Influence of a single fracture on hydraulic fracture propagation.

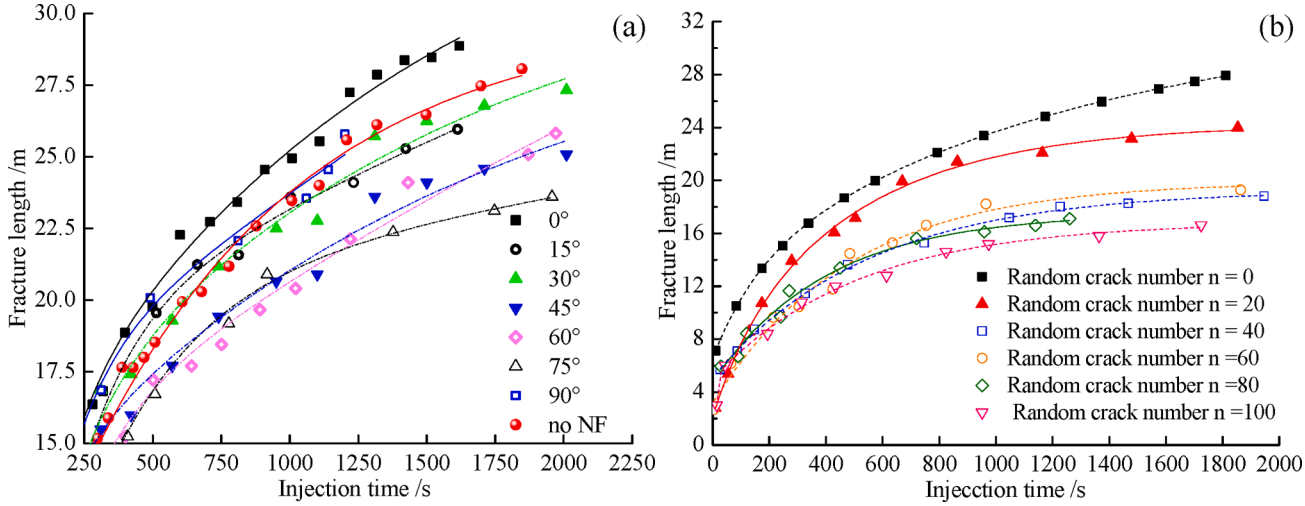

Fig. 13. Effect of approach angles and random fracture number on hydraulic fracture length.

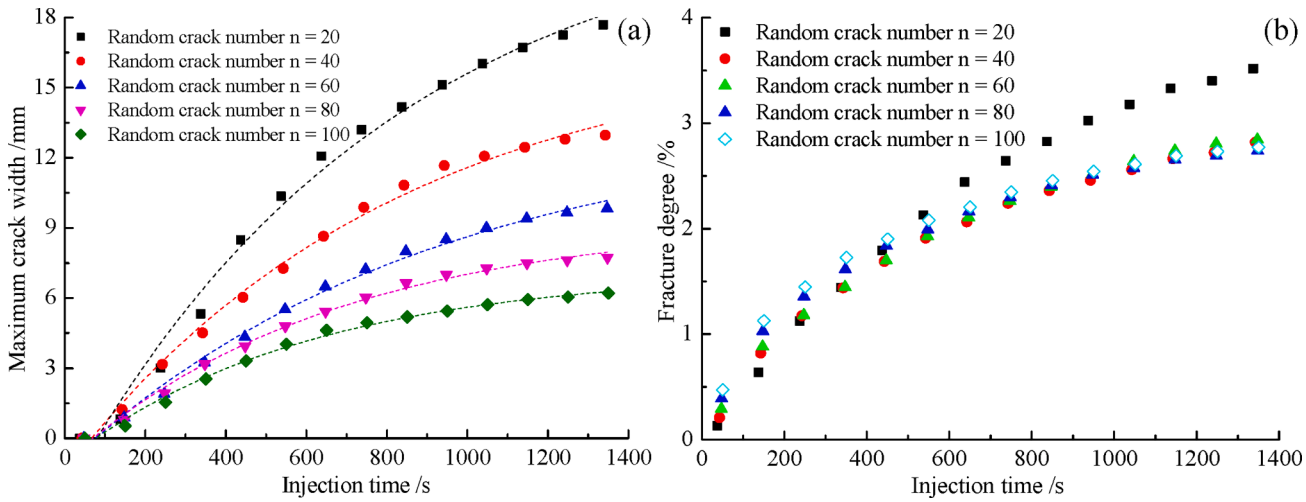

Fig. 14. Effect of random fracture number on maximum fracture width and fracture degree.

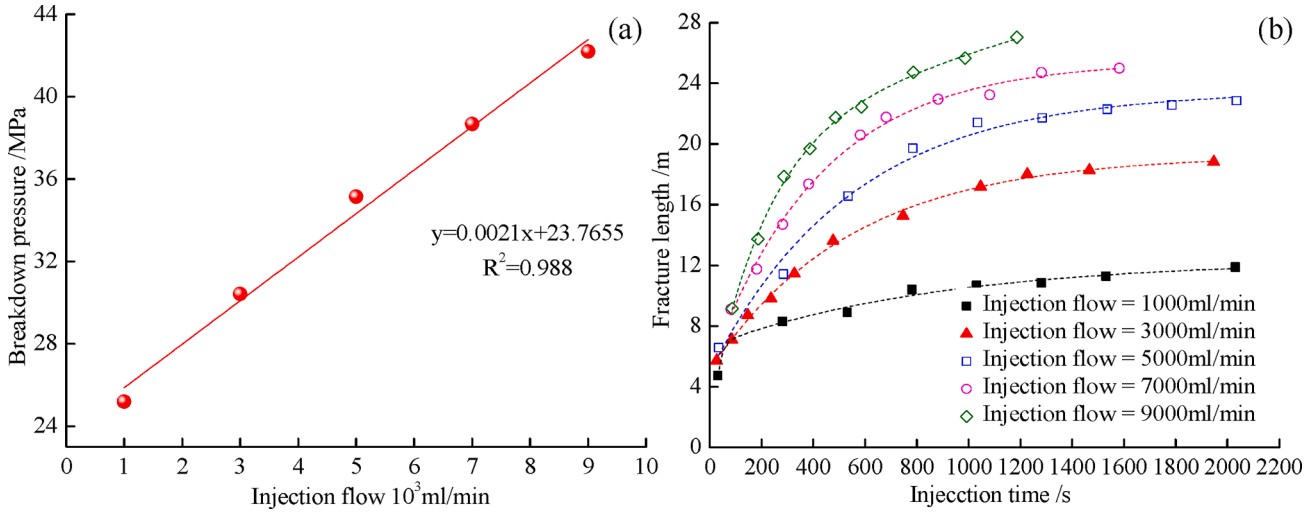

Fig. 15. Variation in breakdown pressure and fracture length with flow.

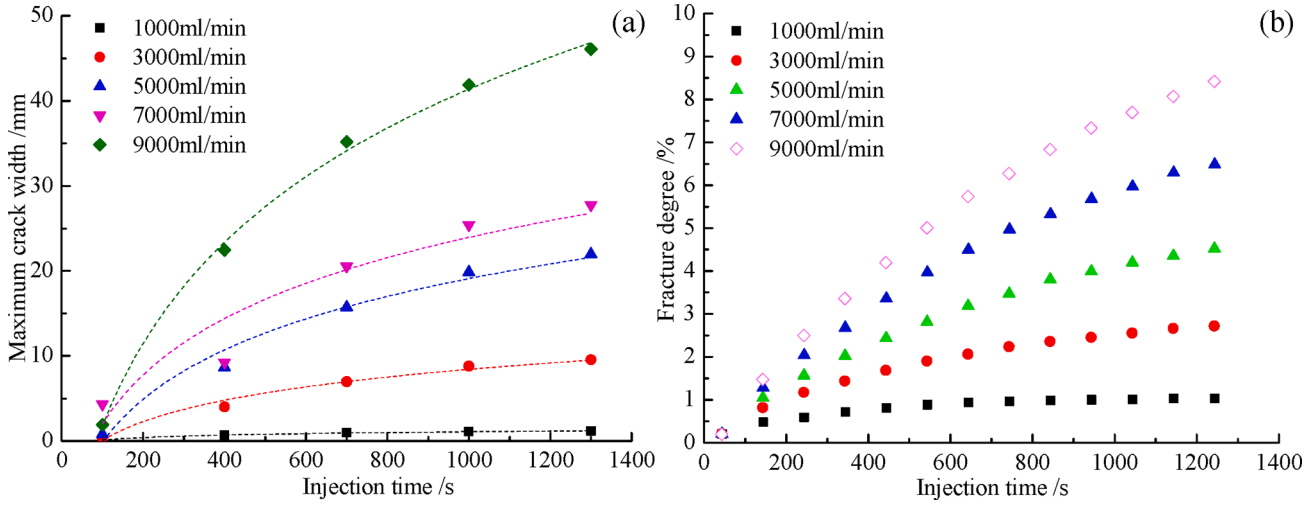

Fig. 16. Variation in the maximum crack width and fracture degree with injection flow.

experiments (Liu et al., 2018b) pointed out that high fracturing fluid injection flow is one of the main measures to increase hydraulic fractures, which is more consistent with the research in this paper. The paper (Zhou et al. 2016) shows that when using a higher injection rate, fracture propagation requires higher fracture pressure and may form complex fracture geometry. When a low viscosity fluid is used, it is easier for the fluid to penetrate the surrounding rock from the borehole, resulting in a lower fracture pressure. This result is consistent with the content of this study.

4.5. Impact of fracturing fluid viscosity

The in situ stress of the model is set as the three-dimensional stress at a depth of 1000 m, and the number of random fractures is set to 40. Refer to Table 1 for other parameters of the model. The fracturing fluid viscosity is set to 0.001 Pa·s, 0.003 Pa·s, 0.005 Pa·s, 0.007 Pa·s, 0.009 Pa·s, 0.017 Pa·s, 0.061 Pa·s, etc. The numerical analysis results show that an increase in fracturing fluid viscosity will cause significant changes in hydraulic fracture morphology and breakdown pressure. Fig. 17 shows the effect of the change in the shape of the hydraulic fracture with larger

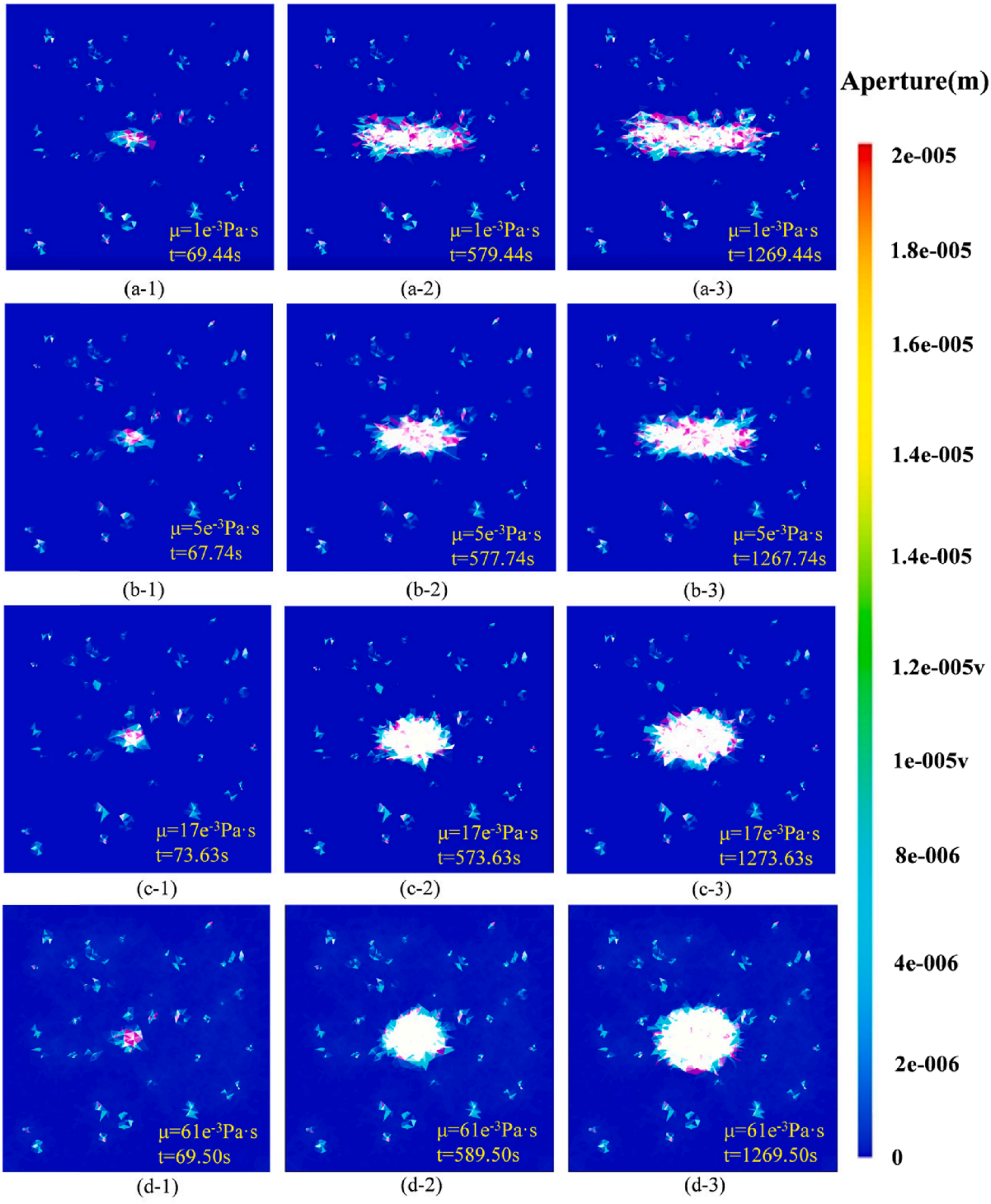

Fig. 17. Effect of fracturing fluid viscosity on hydraulic fracture morphology.

viscosity on the XY plane. With a sharp increase in the viscosity of the fracturing fluid, the shape of the fracture tends to change from elliptical to circular. The increase in fracturing fluid viscosity will cause the stagnation of fracture propagation in coal. Under the same parameter conditions, the fracture length of hydraulic fractures decreases with an increase in viscosity, and the semi-minor axis increases with an increase in viscosity, which contributes to the stagnation of fracture propagation around the wellbore and cannot effectively expand forward.

Fig. 18 shows the breakdown pressure calculated by the models of different fracturing fluid viscosities. With an increase in viscosity, the breakdown pressure increases, and there is a natural exponential correspondence between the breakdown pressure and the viscosity of the fracturing fluid. As shown in Fig. 19(a), the maximum fracture width increases with an increase in viscosity, but the maximum fracture width does not significantly increase when the fracturing fluid viscosity exceeds 0.003 Pa s. As shown in Fig. 19(b), the fracture degree increases exponentially with the time of injection fracturing, but the fracture degree is not significantly affected by the change in viscosity value. (Zhang et al. 2020a) discovered through experiments that CO_2 fracturing fluid with low viscosity has a stronger antireflection effect than water, which is similar to the research findings in this paper. Deng et al. (2018) showed that the proper viscosity of fracturing fluid can promote an increase in fracture diffusion. However, when the viscosity is too high, hydraulic fractures only appear around the wellbore.

5. Discussion

5.1. Volume heterogeneity of the model

According to the concept of volume heterogeneity of rock minerals defined by Zhang yuan et al. (Zhang et al., 2009), volume heterogeneity is defined as the reciprocal of the square sum of the volume content percentage of all mineral components constituting rock minerals, which is expressed as:

$$V_n = 1 \Big/ \sum_{i=1,n} v_i^2 \tag{10}$$

According to this definition, the volume rate of the fracture surface and the volume rate of the homogeneous body outside the fracture surface in this model are denoted as V_1 and V_2, respectively. The volume heterogeneity shown in Table 2 can be calculated according to the randomly generated fracture surface parameters. It can be seen from the above table that the volume heterogeneity of the model is positively correlated with the number of fracture surfaces.

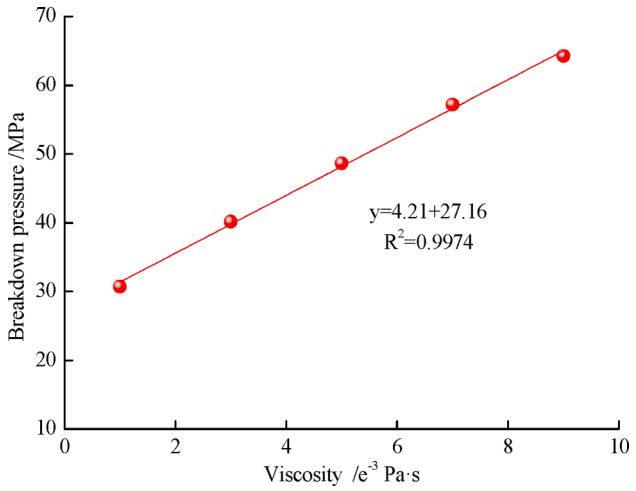

Fig. 18. Variation in breakdown pressure with fracturing fluid viscosity.

5.2. Multi-parameter analysis

The above simulation shows that the fracture length and maximum fracture width have obvious effects on the flow, model volume heterogeneity, buried depth and injection time, while the regularity of the effect of fracturing fluid viscosity on it is inconsistent with the above factors. Through statistical fitting of the model fracture length parameters and maximum fracture width parameters in the above simulation, the data relationship among the simulated fracture length and flow, model volume heterogeneity, buried depth and injection time can be obtained, as shown in Equation (11):

$$L = \frac{\left(-7099.222e^{-\frac{t}{581.631}} + 8981.348\right)Q^{0.331}}{V_n^{1672.801}H^{0.364}} \tag{11}$$

where L is the length of hydraulic fracture, unit: m; t is the injection time, unit: s; Q is the fracturing fluid flow, unit: m^3/s; V_n is the heterogeneity of model volume, without units; is the buried depth, unit: m; and the fitting correlation coefficient $R^2 = 0.958$. According to the above relationship and under the condition of constant flow injection with a Q value of 3000 ml/min, the multi-parameter fitting surface diagram of seam length, model volume heterogeneity, buried depth and injection time can be obtained, as shown in Fig. 20.

Similarly, the data relationship among the maximum fracture width and flow, model volume heterogeneity, buried depth and injection time can be obtained, as shown in Equation (12):

$$D = \frac{\left(-444370.133e^{-\frac{t}{1585.86}} + 425765.250\right)Q^{0.871}}{V_n^{4101.105}H^{1.065}} \tag{12}$$

where D is the width of the hydraulic fracture, unit: m; t is the injection time, unit: s, and the fitting correlation coefficient $R^2 = 0.973$. According to the above relationship and under the condition of constant flow injection with a Q value of 3000 ml/min, the multi-parameter fitting surface diagram of the maximum crack width, model volume heterogeneity, buried depth and injection time can be obtained, as shown in Fig. 21. The above two formulas show that when water is selected as the fracturing fluid, the fracture width is inversely correlated with V_n and H positively correlated with the fracturing fluid flow, which is more consistent with the discussion on fracture length and width in paper (Abdollahipour et al. 2016). In the equation, due to the large index of V_n, the volume inhomogeneity of the model has a large impact on the seam length and width of the maximum hydraulic fracture, and in the specific CBM development, priority is given to selecting the area with simple formation conditions to reduce the impact of reservoir inhomogeneity on the hydraulic fracture (Kresse et al. 2013; Yaobin et al. 2020). The hydraulic fracture width and maximum fracture width are inversely correlated with the burial depth h and positively correlated with the fracturing fluid displacement Q. Therefore, the purpose of accelerating fracturing can be achieved by increasing the displacement (Liu et al., 2018a). The above relationship and diagram reveals that the crack length and width increase with an increase in time, which is consistent with the relationship between the theoretical solution of fracture length and width and time in the KGD model (Abdollahipour et al. 2016).

5.3. Influence of multiple parameters on hydraulic fracture propagation pressure

When the stress difference between the fractured coal seam and the roof (floor) is small, the elastic modulus is an important factor for controlling the longitudinal propagation of the fracture. When the elastic modulus of the hydraulic fracturing formation is less than that of the upper and lower strata and the difference is large, the hydraulic fracture height will be confined to the fracturing layer (Cao et al. 2020; Fu et al. 2019; Fu, Savitski, and Bunger 2018). In this model, considering that the roof of the Qin-shui basin #15 coal seam is a thick limestone and

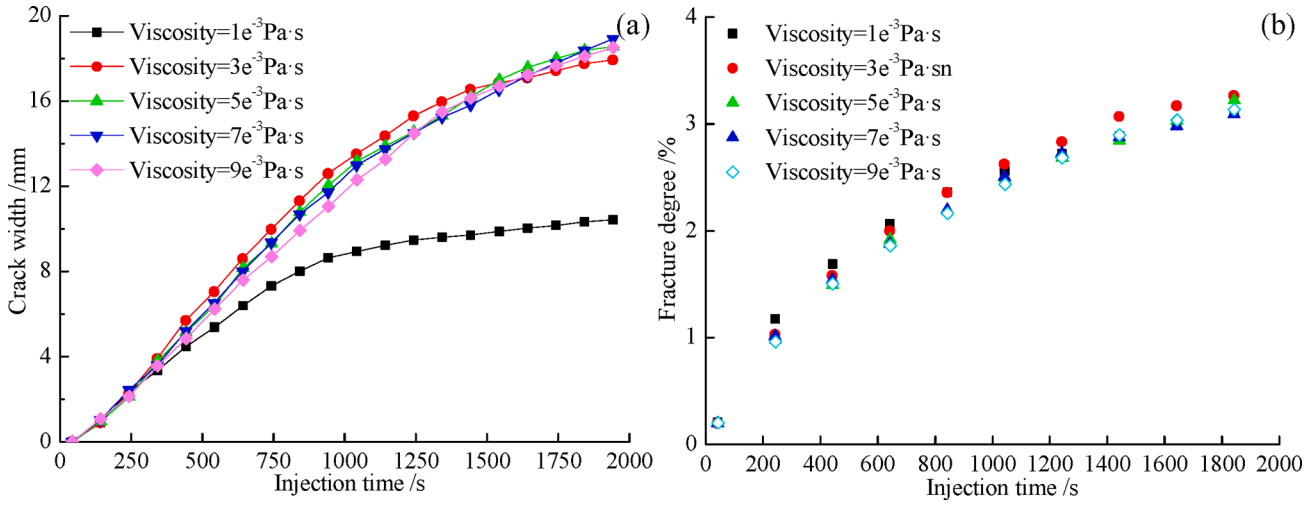

Fig. 19. Variation in the maximum fracture width and fracture degree curve with fracturing fluid viscosity.

Table 2
Calculation of the degree of heterogeneity in the model.

n	V_1	V_2	V_1^2	V_2^2	V_n
0	0	1	0	1	1
20	3.19379E-05	0.999968062	2.55007E-12	0.999996806	1.000063878
40	6.38757E-05	0.999936124	1.02003E-09	0.999936125	1.00012776
60	9.58136E-05	0.999904186	4.08011E-09	0.999872253	1.000191646
80	0.000127751	0.999872249	9.18025E-09	0.999808382	1.000255536
100	0.000159689	0.999840311	1.63204E-08	0.999744513	1.00031943

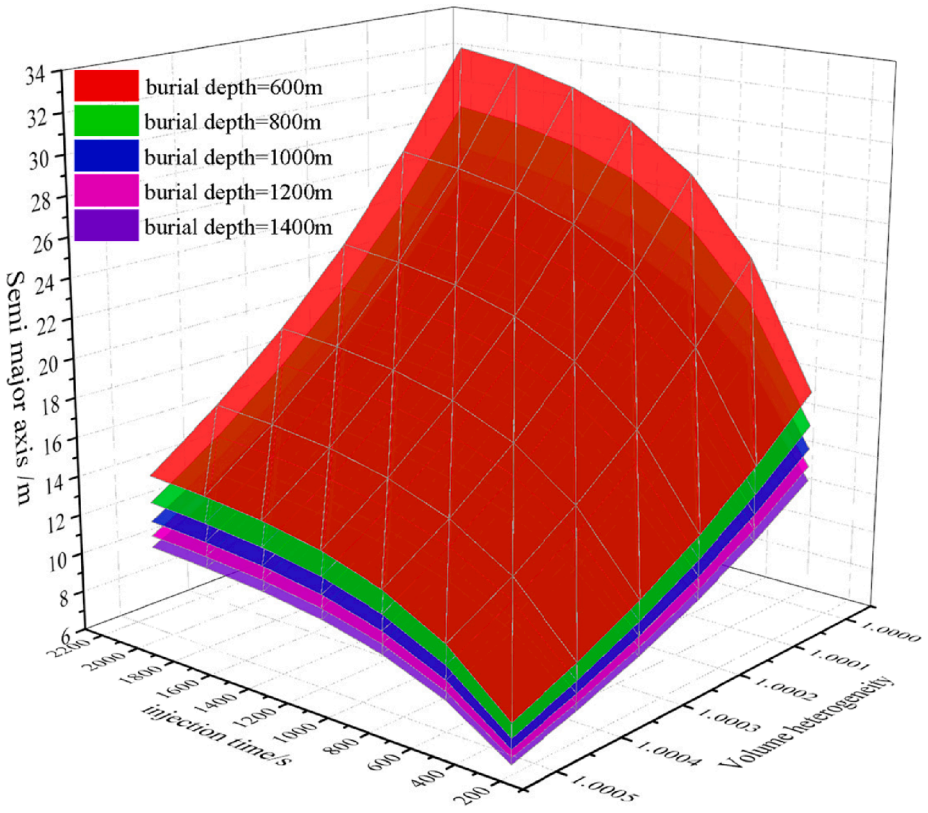

Fig. 20. Relationship between fracture length and multiple factors under constant flow injection.

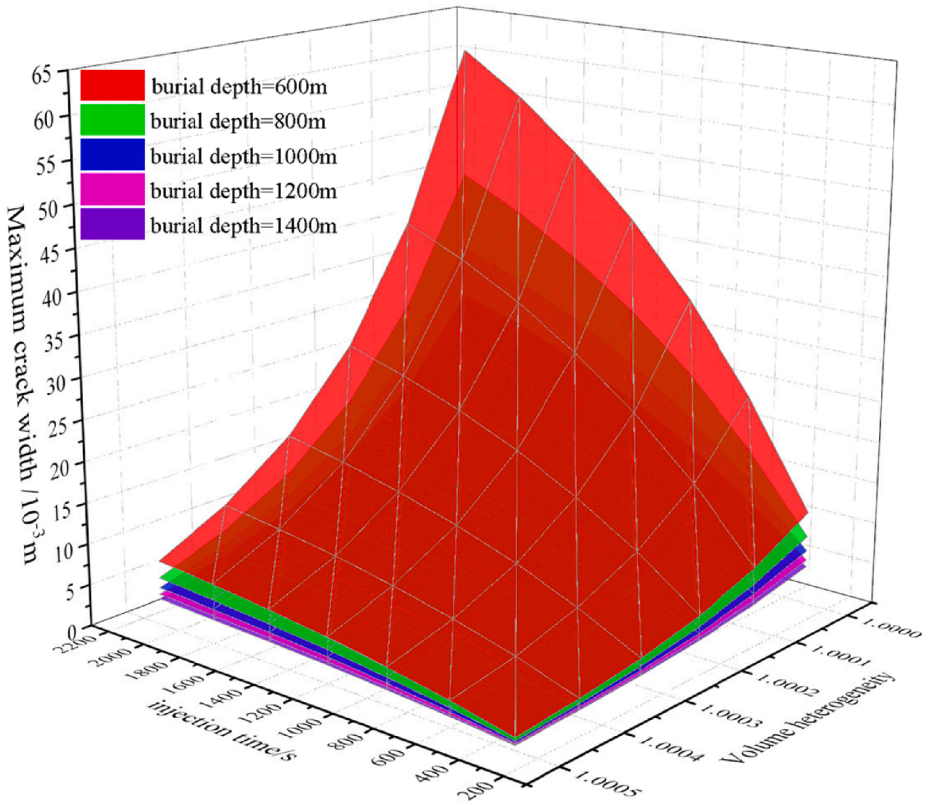

Fig. 21. Relationship between the maximum fracture width and multiple factors under constant flow injection.

its floor is a thick siltstone, the average elastic model of these two layers of hard rocks is 2.92 times and 1.49 times, respectively, that of the coal seam. According to the theoretical analysis, hydraulic fractures should be limited to coal reservoirs with relatively low strength, so this model is set as a single-layer hydraulic fracturing model. The simulation results show that in the z-axis direction, the crack height can penetrate into the up and down interfaces in a short time, and the fracture height is confined between the up layer and down layer. In the XY plane, the hydraulic fracture expands along the direction of the maximum principal stress and along the x-axis in this model and has a short length in the y-axis direction. As shown in Fig. 22, the expansion form of hydraulic fractures in the XY plane is similar to an ellipse. This finding is consistent with the research conclusion of paper (N. Li et al. 2021). It can be seen that the fracture expands to both ends in the X direction with an increase in time and that the expansion range in the Y direction decreases with an increase in time. The fracture width does not infinitely expand but will reach a limit value. From the point of view of stress, the action of water pressure will lead to the displacement of solid media on both sides of the fracture, causing an increase in the stress value in the direction of minimum principal stress until the stress in the direction of the water pressure and minimum principal stress reach equilibrium (Bai et al. 2020; Ju et al., 2018a).

According to the theory of coal seam breakdown pressure under the action of cylindrical nonuniform horizontal stress, that is, the theory of the elliptical hole model, when the edge of the elliptical hole is under the action of uniform pressure P_1, the maximum horizontal normal stress at the end of the long axis is expressed as follows:

$$\sigma_{max} = \left(2\frac{a}{b} - 1\right)P_1 \tag{13}$$

where a is the semi-major axis of the ellipse and b is the semi-minor axis of the ellipse.

According to the theory of elasticity, when the semi-major axis and semi-minor axis of the ellipse are equal, that is, when $a = b$, P_1 is the breakdown pressure. On the boundary of the circular hole, the maximum normal stress of the material is less than or equal to the water pressure P_1, and only when the fracture occurs is the normal stress at the fracture point equal to the water pressure. After the rock mass is broken, the fracture shape quickly changes from circular to elliptical, and the fracture fluid pressure drops significantly to the treatment pressure P_2. At this time, a is much greater than b, and the maximum horizontal normal stress σ'_{max} in Equation (14) is less than or equal to the treatment

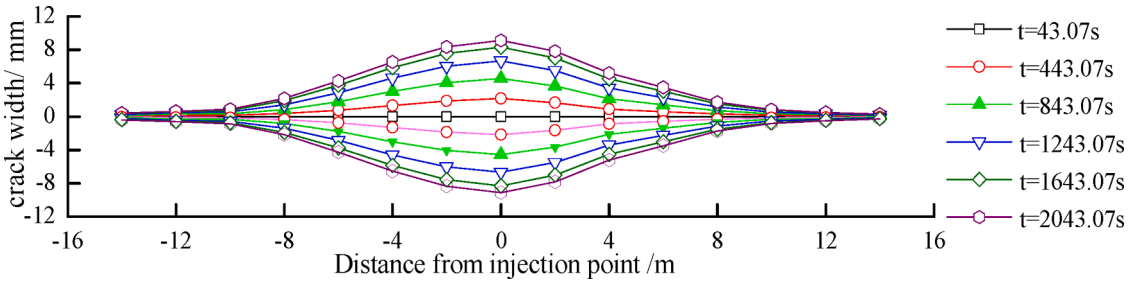

Fig. 22. Variation in hydraulic fracture shape with injection time.

pressure P_2 of the hydraulic fracture, that is, it satisfies the following equation:

$$P_2 \geqslant \sigma'_{max} \tag{14}$$

According to the maximum normal stress theory, the maximum normal stress $\sigma'_{\max}$ occurs at the end of the semi-major axis of the ellipse. When the maximum normal stress $\sigma'_{\max}$ reaches the yield normal stress of the material in a simple tensile specimen (Formula 15), the fracture occurs, and the hydraulic fracture continues to expand.

$$\sigma'_{max} \geqslant \sigma_\tau \tag{15}$$

where $\sigma'_{\max}$ is the normal stress at the end of the semi-major axis of the ellipse and σ_τ is the tensile strength of the material.

In deep strata, the fracture tip is also affected by the minimum principal stress of the rock mass during the continuous propagation of hydraulic fractures. The direction of the normal stress at the end of the semi-major axis of the minimum principal stress ellipse is opposite. Therefore, the above formula should be corrected as:

$$\sigma'_{max} \geqslant \sigma_\tau + \sigma_h \tag{16}$$

According to relationship 14 and relationship 16, the following relationship holds:

$$P_2 \geqslant \sigma_\tau + \sigma_h \tag{17}$$

The above formula is the relationship between the treatment pressure near the wellbore and the tensile strength of the material. In the process of extension away from the wellbore, the water pressure also incurs the loss of friction resistance. Therefore, the above formula should be corrected as.

$$P_2 \geqslant \sigma_\tau + \sigma_h + \Delta P_f \tag{18}$$

where $\triangle P_f$ is the frictional resistance loss from the wellbore to the fracture tip. Therefore, the treatment pressure P_2 is the pressure that determines the continuous expansion of hydraulic fractures.

Fig. 23(a) shows a typical fracturing curve. The propagation pressure of hydraulic fractures is the pressure after the breakdown pressure decreases and tends to stabilize. According to the mechanical conditions of coal seam cracking and expansion, the hydrostatic pressure acting on the borehole wall is greater than the sum of the cohesive force and minimum principal stress of the coal reservoir (Zou et al. 2017). Therefore, whether the hydraulic fracture can continue to expand forward depends on the treatment pressure. Fig. 23(b) shows the variation trend of the treatment pressure for the above model with burial depth, and the breakdown pressure increases with an increase in burial depth because the minimum principal stress value also increases with an increase in burial depth. Fig. 23(c) shows the variation curve of different injection flows to treatment pressures with burial depth, where the breakdown pressure increases with an increase in injection flow. Fig. 23(d) shows the variation curve of treatment pressure under the condition of different numbers of fracture surfaces, and the treatment pressure decreases with an increase in volume heterogeneity (Dou et al. 2019; Wu et al. 2022). Hydraulic fractures are more prone to cause fracturing fluid filtration when passing through fault structures, resulting in a pressure drop and hindering fracture expansion (Ju et al. 2016; Kresse et al. 2013; Li et al. 2020; Yan and Zheng 2017). Therefore, the reservoir volume heterogeneity, burial depth and fracturing fluid flow are the main

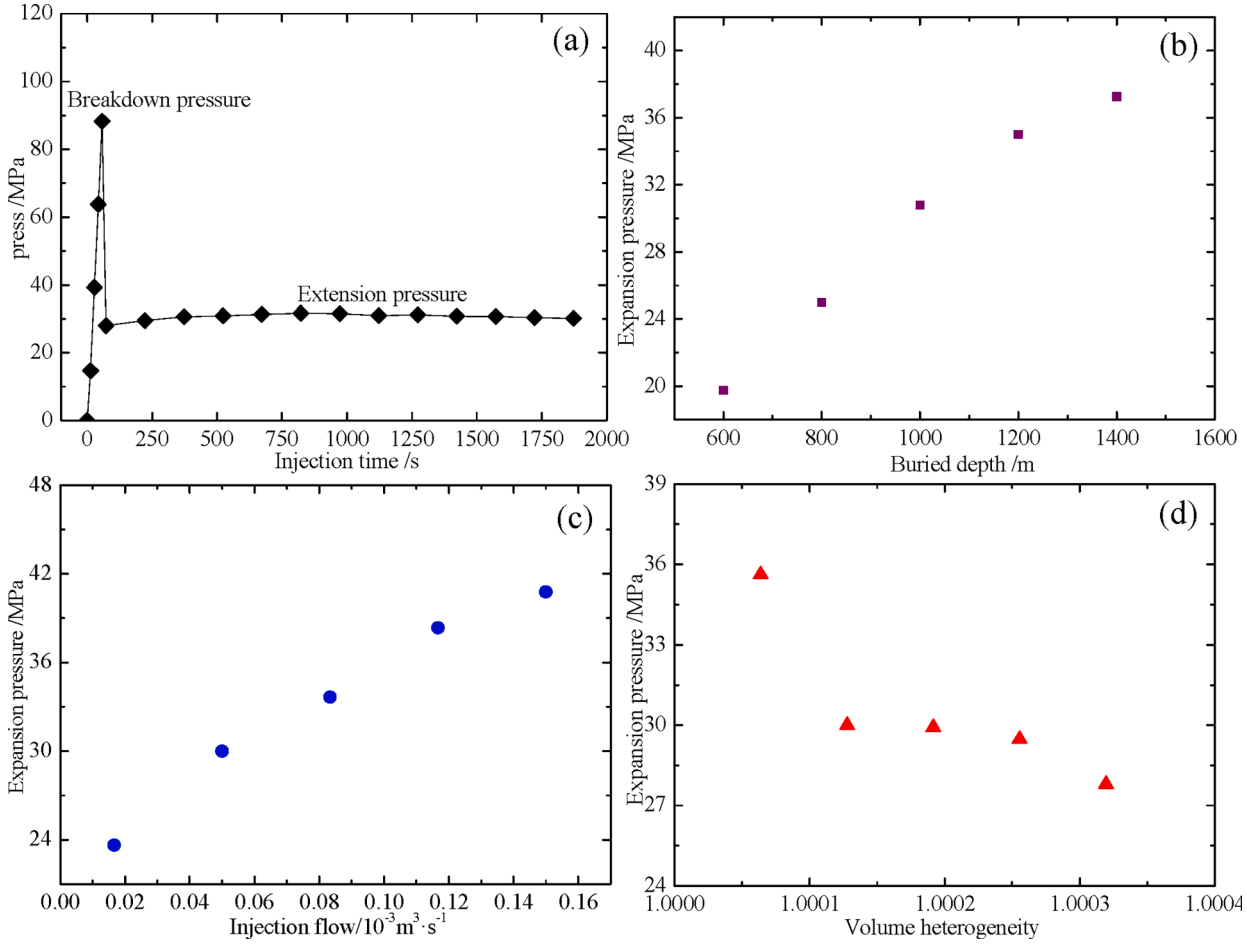

Fig. 23. Variation curve of the treatment pressure at the injection point (a) Schematic of treatment pressure; (b) Influence of buried depth on spreading pressure; (c) Effect of fracturing fluid flow on treatment pressure; (d) Influence of volume heterogeneity on treatment pressure.

controlling factors affecting the expansion of hydraulic fractures in a specific CBM reservoir. The above factors control the expansion of hydraulic fractures by affecting the treatment pressure of the fracturing fluid.

6. Conclusion

In this paper, a numerical analysis model of hydraulic fracturing in a deep coal reservoir with random fractures is established by using continuous and discontinuous algorithm software. The effects of burial depth, number of fracture surfaces, injection flow and viscosity on the propagation shape, fracture length and maximum fracture width of three-dimensional hydraulic fractures in coal reservoirs are investigated by the controlling variable method. The main findings are presented as follows:

(1) The discrete fracture network model is employed to model the heterogeneous deep coal and rock mass, and the continuous discontinuous numerical algorithm is utilized to realize the numerical calculation of the hydraulic fracture shape and propagation law of deep coal and rock mass. The effects of different numbers of random fractures, burial depths (in-situ stress), fracturing fluid flow and fracturing fluid viscosity on the hydraulic fracture morphology, breakdown pressure, fracture length and maximum fracture width of coal reservoirs are investigated by the control variable method.
(2) The concept of volume heterogeneity is defined. Through multiple regression analysis, it is concluded that when water is used as the fracturing fluid, coal reservoir volume heterogeneity, burial depth (in-situ stress) and fracturing fluid flow are the main controlling factors affecting fracture length and maximum fracture width. The fracture length and maximum fracture width are inversely correlated with the power value of volume heterogeneity and burial depth and positively correlated with the power value of injection flow and injection time.
(3) The relationship between the hydraulic fracture propagation pressure and the tensile strength of coal and rock mass is explored, and the effects of the above factors on the fracturing fluid propagation pressure are discussed. It is verified that the reservoir volume heterogeneity, burial depth and fracturing fluid flow are important control factors for hydraulic fracture propagation in coalbed methane reservoirs.
(4) The viscosity of fracturing fluid also has an important impact on the hydraulic fracture morphology and fracture characteristic parameters in coal reservoirs. The increase in viscosity hinders fracture propagation, and the fracture width does not continuously increase. In the hydraulic fracturing of coalbed methane reservoirs, the use of relatively low viscosity fracturing fluid is considered with the premise of meeting the needs of other projects.

Declaration of Competing Interest

The authors declare that they have no known competing financial interests or personal relationships that could have appeared to influence the work reported in this paper.

Data availability

The authors do not have permission to share data.

Acknowledgments

Financial support for this study is provided by the National Natural Science Foundation of China (Nos. U1910206, 51874312, 51861145403), Science and Technology Plant Project of Inner Mongolia Autonomous Region (2019GG140), Major Scientific and Technological Innovation Project of Shandong Province (Nos. 2019SDZY01, 2019SDZY02), and Beijing Municipal Natural Science Foundation (8184082).

References

Abdollahipour, A., Marji, M.F., Bafghi, A.Y., Gholamnejad, J., 2016. DEM simulation of confining pressure effects on crack opening displacement in hydraulic fracturing. Int. J. Mining Sci. Technol. 26 (4), 557–561. https://doi.org/10.1016/j.ijmst.2016.05.004.

Ai, C., Li, X.-X., Zhang, J., Jia, D., Tan, W.-J., 2018. Experimental investigation of propagation mechanisms and fracture morphology for coalbed methane reservoirs. Pet. Sci. 15 (4), 815–829.

Bai, Q., Liu, Z., Zhang, C., Wang, F., 2020. Computers and geotechnics geometry nature of hydraulic fracture propagation from oriented perforations and implications for directional hydraulic fracturing. Comput. Geotech. 125 (January), 103682 https://doi.org/10.1016/j.compgeo.2020.103682.

Cao, S., Li, X., Zhou, Z., Wang, Y., Ding, H., 2020. Investigation of hydraulic fracturing crack propagation behavior in multi-layered coal seams. Appl. Sci. (Switzerland) 10 (3), 1153.

Carrier, B., Granet, S., 2012. Numerical modeling of hydraulic fracture problem in permeable medium using cohesive zone model. Eng. Fract. Mech. 79, 312–328. https://doi.org/10.1016/j.engfracmech.2011.11.012.

Chen, Z., 2012. Finite element modelling of viscosity-dominated hydraulic fractures. J. Petrol. Sci. Eng. 88–89, 136–144. https://doi.org/10.1016/j.petrol.2011.12.021.

Chen, Z., Jeffrey, R.G., Zhang, X.i., Kear, J., 2017. Finite-element simulation of a hydraulic fracture interacting with a natural fracture. SPE J. 22 (1), 219–234.

Cheng, Y., Lu, Y., Ge, Z., Cheng, L., Zheng, J., Zhang, W., 2018. Experimental study on crack propagation control and mechanism analysis of directional hydraulic fracturing. Fuel 218, 316–324.

Chong, Z., et al., 2017. 10 Energies numerical investigation into the effect of natural fracture density on hydraulic fracture network propagation.

Chuang, L., Huamin, L.i., Dongjie, J., 2017. Numerical simulation study on the relationship between mining heights and shield resistance in longwall panel. Int. J. Mining Sci. Technol. 27 (2), 293–297. https://doi.org/10.1016/j.ijmst.2017.01.017.

Dahi-taleghani, A., Jon E.O., 2011. Numerical modeling of multistranded- hydraulic-fracture propagation : accounting for the interaction between induced and natural fractures. (September): 575–81.

de Pater, C.J., 2015, Hydraulic fracture containment: new insights into mapped geometry. SPE in "Hydraulic Fracturing Technology Conference held in The Woodlands. Texas, USA 3-5- February 2015, paper SPE.173359-MS.

Deng, B., Yin, G., Li, M., Zhang, D., Lu, J., Liu, Y., Chen, J., 2018. Feature of fractures induced by hydrofracturing treatment using water and L-CO_2 as fracturing fluids in laboratory experiments. Fuel 226, 35–46.

Dontsov, E.V., Zhang, F., 2018. Calibration of tensile strength to model fracture toughness with distinct element method. Int. J. Solids Struct. 144–155, 180–191.

Dou, F., Wang, J.G., Wang, H., Hu, B., Li, C., 2019. Discrete element analysis for hydraulic fracture propagations in laminated reservoirs with complex initial joint properties. Geofluids 2019, 1–23.

Fu, W., Savitski, A.A., Bunger, A.P., 2018. Analytical criterion predicting the impact of natural fracture strength, height and cemented portion on hydraulic fracture growth. Eng. Fract. Mech. 204 (February), 497–516. https://doi.org/10.1016/j.engfracmech.2018.10.002.

Fu, W., Savitski, A.A., Damjanac, B., Bunger, A.P., 2019. Three-dimensional lattice simulation of hydraulic fracture interaction with natural fractures. Comput. Geotech. 107 (December 2018), 214–234. https://doi.org/10.1016/j.compgeo.2018.11.023.

Huang, B., Chen, S., Zhao, X., 2017a. Hydraulic fracturing stress transfer methods to control the strong strata behaviours in gob-side gateroads of longwall mines. Arabian J. Geosci. 10 (11).

Huang, S., Liu, D., Yao, Y., Gan, Q., Cai, Y., Xu, L., 2017b. Natural fractures initiation and fracture type prediction in coal reservoir under different in-situ stresses during hydraulic fracturing. J. Nat. Gas Sci. Eng. 43, 69–80.

Jiang, T., Zhang, J., Hao, W.u., 2016. Experimental and numerical study on hydraulic fracture propagation in coalbed methane reservoir. J. Nat. Gas Sci. Eng. 35, 455–467. https://doi.org/10.1016/j.jngse.2016.08.077.

Jiang, T., Ye, H., Ren, G., Zhang, J., Li, Y., Wang, J., Wu, H., Zhang, C., Huang, G., Ke, B. o., Liu, W., 2019. Crack initiation and propagation in coalbed gas reservoir during hydraulic fracturing. Sadhana – Acad. Proc. Eng. Sci. 44 (2).

Ju, Y., Liu, P., Chen, J., Yang, Y., Ranjith, P.G., 2016. CDEM-based analysis of the 3D initiation and propagation of hydrofracturing cracks in heterogeneous glutenites. J. Nat. Gas Sci. Eng. 35, 614–623.

Ju, Y., Chen, J., Wang, Y., Gao, F., Xie, H., 2018a. Numerical analysis of hydrofracturing behaviors and mechanisms of heterogeneous reservoir glutenite, using the continuum-based discrete element method while considering hydromechanical coupling and leak-off effects. J. Geophys. Res. Solid Earth 123 (5), 3621–3644.

Ju, Y., Wang, Y., Dong, H., Yang, Y., 2018b. Numerical analysis of the hydrofracturing behaviour of heterogeneous glutenite considering hydro-mechanical coupling effects based on bonded particle models. Int. J. Numer. Anal. Meth. Geomech. 42 (13), 1493–1515.

Jung, A., Fenwick, D.H., Caers, J., 2013. Training image-based scenario modeling of fractured reservoirs for flow uncertainty quantification. Comput. Geosci. 17 (6), 1015–1031.

Kresse, O., Weng, X., Hongren, G.u., Ruiting, W.u., 2013. Numerical modeling of hydraulic fractures interaction in complex naturally fractured formations. Rock Mech. Rock Eng. 46 (3), 555–568.
Lecampion, B., Detournay, E., 2007. An implicit algorithm for the propagation of a hydraulic fracture with a fluid lag. Comput. Methods Appl. Mech. Eng. 196 (49–52), 4863–4880.
Li, N., Fang, L., Sun, W., Zhang, X., Chen, D., 2021. Evaluation of borehole hydraulic fracturing in coal seam using the microseismic monitoring method. Rock Mech. Rock Eng. 54 (2), 607–625.
Li, Z.-Q., Li, X.-L., Yu, J.-B., Cao, W.-D., Liu, Z.-F., Wang, M., Liu, Z.-F., Wang, X.-H., 2020. Influence of existing natural fractures and beddings on the formation of fracture network during hydraulic fracturing based on the extended finite element method. Geomech. Geophys. Geo-Energy Geo-Resources 6 (4). https://doi.org/10.1007/s40948-020-00180-y.
Li, Z., Wang, J., Li, L., Wang, L., Liang, R.Y., 2015. A case study integrating numerical simulation and GB-InSAR monitoring to analyze flexural toppling of an anti-dip slope in fushun open pit. Eng. Geol. 197, 20–32.
Lin, Q., Feng, C., Zhu, X., Zhang, G., Li, S., 2021. Evolution characteristics of crack and energy of low-grade highway under impact load. Int. J. Pavement Eng. 23 (9), 3182–3197.
Liu, D., Shi, X., Zhang, X., Wang, B., Tang, T., Han, W., 2018a. Hydraulic fracturing test with prefabricated crack on anisotropic shale: laboratory testing and numerical simulation. J. Petrol. Sci. Eng. 168, 409–418.
Liu, J., Yao, Y., Liu, D., Xu, L., Elsworth, D., Huang, S., Luo, W., 2018b. Experimental simulation of the hydraulic fracture propagation in an anthracite coal reservoir in the southern Qin-shui Basin, China. J. Petrol. Sci. Eng. 168, 400–408.
Lyu, S., Wang, S., Chen, X., Wang, S., Wang, T., Shi, X., Dong, Q., Li, J., 2020. Natural fractures in soft coal seams and their effect on hydraulic fracture propagation: a field study. J. Petrol. Sci. Eng. 192, 107255.
Ma, Z., Feng, C., Liu, T., Li, S., 2011. A GPU accelerated continuous-based discrete element method for elastodynamics analysis. Adv. Mater. Res. 320, 329–334.
Ma, K., Tang, C.A., Wang, L.X., Tang, D.H., Zhuang, D.Y., Zhang, Q.B., Zhao, J., 2016. Stability analysis of underground oil storage caverns by an integrated numerical and microseismic monitoring approach. Tunn. Undergr. Space Technol. 54, 81–91.
Marongiu-Porcu, M., Lee, D., Shan, D., Morales, A., 2016. Advanced modeling of interwell-fracturing interference: an eagle ford shale-oil study. SPE J. 21 (5), 1567–1582.
Palmer, I., 2010. Coalbed methane completions: a world view. Int. J. Coal Geol. 82 (3–4), 184–195. https://doi.org/10.1016/j.coal.2009.12.010.
Peng, W., Xian-biao, M., Jin-bin, L., Chun-zhi, D.u., 2009. Study of the borehole hydraulic fracturing and the principle of gas seepage in the coal seam. Procedia Earth Planet. Sci. 1 (1), 1561–1573. https://doi.org/10.1016/j.proeps.2009.09.241.
Ren, F., Ma, G., Fan, L., Wang, Y., Zhu, H., 2017. Equivalent discrete fracture networks for modelling fluid flow in highly fractured rock mass. Eng. Geol. 229, 21–30.
Tan, P., Jin, Y., Han, K., Hou, B., Guo, X., Gao, J., Wang, T., 2017. Analysis of hydraulic fracture initiation and vertical propagation behavior in laminated shale formation. Fuel 206, 482–493. https://doi.org/10.1016/j.fuel.2017.05.033.
Wang, H.Y., 2019. Hydraulic fracture propagation in naturally fractured reservoirs: complex fracture or fracture networks. J. Nat. Gas Sci. Eng. 68 (August 2018), 102911. https://doi.org/10.1016/j.jngse.2019.102911.
Wang, H., Bai, C., Feng, C., Xue, K., Zhu, X., 2019. An efficient CDEM-based method to calculate full-scale fragment field of warhead. Int. J. Impact Eng. 133, 103331.
Wang, S., Li, H., Li, D., 2018. Numerical simulation of hydraulic fracture propagation in coal seams with discontinuous natural fracture networks. Processes 6 (8), 113.
Wang, Y., Liu, D., Cai, Y., Yao, Y., Pan, Z., 2020. Constraining coalbed methane reservoir petrophysical and mechanical properties through a new coal structure index in the Southern Qin-shui Basin, Northern China: implications for hydraulic fracturing. AAPG Bull. 104 (8), 1817–1842.
Wanniarachchi, W., Gamage, R., Perera, M., Rathnaweera, T., Gao, M., Padmanabhan, E., 2017. Investigation of depth and injection pressure effects on breakdown pressure and fracture permeability of shale reservoirs: an experimental study. Appl. Sci. (Switzerland) 7 (7), 664.
Wu, M., Gao, K.e., Liu, J., Song, Z., Huang, X., 2022. Influence of rock heterogeneity on hydraulic fracturing: A parametric study using the combined finite-discrete element method. Int. J. Solids Struct. 234-235, 111293.
Wu, J., Zhang, S., Cao, H., Zheng, M., Qu, F., Peng, C., 2020. xperimental investigation of crack dynamic evolution induced by pulsating hydraulic fracturing in coalbed methane reservoir 1. J. Nat. Gas Sci. Eng. 75, 103159.
Yan, C., Zheng, H., 2017. FDEM-Flow3D: a 3D hydro-mechanical coupled model considering the pore seepage of rock matrix for simulating three-dimensional hydraulic fracturing. Comput. Geotech. 81, 212–228. https://doi.org/10.1016/j.compgeo.2016.08.014.
Yaobin, S., Weiyong, L.u., Changchun, H.e., Erhu, B., 2020. Numerical simulation of the influence of natural fractures on hydraulic fracture propagation. Geofluids 2020, 1–12.
Zhang, X., Caifang, W.u., Wang, Z., Dongjing, X.u., 2019. Postfracturing permeability prediction for CBM well with the analysis of fracturing pressure decline. Energy Sci. Eng. 7 (6), 3111–3123.
Zhang, Z., Li, X., He, J., Wu, Y., Zhang, B.o., 2015. Numerical analysis on the stability of hydraulic fracture propagation. Energies 8 (9), 9860–9877.
Zhang, J., Li, Y.-W., Li, W., Chen, Z.-J., Zhao, Y., Yu, F.-H., Zheng, Y., 2020a. Study on propagation behaviors of hydraulic fracture network in tight sandstone formation with closed cemented natural fractures. Geofluids 2020, 1–22.
Zhang, P., Meng, Z., Jiang, S.u., Chen, X., 2020b. Characteristics of in-situ stress distribution in Zhengzhuang Region, Southern Qin-shui Basin, China and its stress path during depletion. Eng. Geol. 264 (February 2019), 105413. https://doi.org/10.1016/j.enggeo.2019.105413.
Zhang, Y., Zhao, Y.S., 2009. Analysis of correlation of rock thermal cracking with inhomogeneity. J. Lanzhou Univ. Technol. (6), 135–137. https://doi.org/10.16285/j.rsm.2011.03.014.
Zhaoxia, D.A.I, Beilei, S.U.N., Fangui, Z., 2020. Geostress characteristics of coal reservoir at Changzhi Block of Southern Qin-shui Basin.
Zhou, J., Zhang, L., Braun, A., Han, Z., 2016. Numerical modeling and investigation of fluid-driven fracture propagation in reservoirs based on a modified fluid-mechanically coupled model in two-dimensional particle flow code. Energies 9 (9), 699.
Zhu, X., Feng, C., Cheng, P., Wang, X., Li, S., 2021. A novel three-dimensional hydraulic fracturing model based on continuum-discontinuum element method. Comput. Methods Appl. Mech. Eng. 383, 113887.
Zou, J., Chen, W., Yuan, J., Yang, D., Yang, J., 2017. 3-D numerical simulation of hydraulic fracturing in a CBM reservoir. J. Nat. Gas Sci. Eng. 37, 386–396.